

Jan Wyndorps

# Investigation of Compression Ignition Combustion of Glycerol-Diesel Emulsions

Master's thesis in Energy Engineering

Supervisor: David Emberson

October 2019



Jan Wyndorps

# **Investigation of Compression Ignition Combustion of Glycerol-Diesel Emulsions**

Master's thesis in Energy Engineering  
Supervisor: David Emberson  
October 2019

Norwegian University of Science and Technology  
Faculty of Engineering  
Department of Energy and Process Engineering



Norwegian University of  
Science and Technology



## *Abstract*

With Biodiesel production having established in the past century, there is an ongoing interest to add value to its abundant by-product glycerol. With regard to a shortly closed product cycle, its utilisation in the fuel sector is favourable. Beside the usage as a stand-alone fuel and chemical conversions to tailor-made oxygenated fuel blends, purified glycerol can be added to diesel fuel in form of an emulsion. The increased oxygen content of the fuel is promising to reduce soot formation when used in compression ignition engines. The objective of this work is the profound investigation of the combustion behaviour of glycerol-diesel emulsions when used as a diesel fuel.

To begin with, previous studies on glycerol utilisation in internal combustion engines are summarised. Based on this knowledge the emulsion preparation method is determined and potential issues due to the properties of glycerol are identified. To obtain a broad view, the experimental investigation is conducted on two independent setups. Global parameters like performance and engine-out emissions are assessed with an instrumented six-cylinder engine which is equipped with a particulate matter and an exhaust gas analyser. Additionally, an optical accessible one-cylinder engine is used for profound investigation of flame properties and in-flame soot using  $\text{OH}^*$ -chemiluminescence and light extinction high-speed imaging. The data acquired on both test rigs are analysed in detail to gain a greater understanding of the combustion properties. In the end, the results are discussed with regard to potential benefits and issues when using glycerol-diesel emulsions.



## *Acknowledgements*

I would like to offer my special thanks to my supervisor Dr. Emberson for his assistance throughout my thesis. His advice and enthusiasm for the project have been a great help. I would also like to express my very great appreciation to Mr. Bjørgen for his assistance in the laboratory and our constructive discussions about post-processing the optical measurements.

I wish to acknowledge the help provided by Professor Løvås whose support and organisation kept the progress on schedule.

I also would like to thank Dr. Beeckmann for our monthly correspondence. His feedback and scientific support was greatly appreciated.

Finally, I wish to thank the whole Combustion Kinetics research group for making the work joyful and keeping the motivation level high.





# Contents

<b>Abstract</b>	<b>iii</b>
<b>Acknowledgements</b>	<b>v</b>
<b>1 Introduction</b>	<b>1</b>
<b>2 Fundamentals</b>	<b>3</b>
2.1 Soot Formation in Compression-Ignition Engines . . . . .	3
2.1.1 Chemically Effective Fuel Properties . . . . .	4
2.1.2 Physically Effective Fuel Properties . . . . .	5
2.2 Glycerol as a Fuel . . . . .	7
2.2.1 Glycerol General Information . . . . .	7
2.2.2 Glycerol as a By-Product of Biodiesel Production . . . . .	8
2.2.3 Pure Glycerol Combustion . . . . .	8
2.2.4 Glycerol Diesel Emulsions . . . . .	9
<b>3 Experimental Setup</b>	<b>11</b>
3.1 Fuel Preparation . . . . .	11
3.1.1 Emulsion Preparation . . . . .	11
3.1.2 Fuel Composition . . . . .	13
3.2 Instrumented Six-Cylinder Engine . . . . .	14
3.3 Optical Accessible One-Cylinder Engine . . . . .	16
3.3.1 Mechanical Setup . . . . .	16
3.3.2 Estimation of In-Cylinder Conditions . . . . .	17
3.3.3 Optical Methods . . . . .	18
3.3.4 Optical Setup . . . . .	19
3.3.5 Non-Ideal Camera Characteristics . . . . .	21
<b>4 Instrumented Engine Results</b>	<b>25</b>
4.1 Instrumented Engine Test Conditions . . . . .	25
4.2 Combustion Behaviour . . . . .	26
4.3 Emissions . . . . .	28
4.3.1 Particulate Matter Emissions . . . . .	28
4.3.2 Gaseous Emissions . . . . .	32
<b>5 Optical Engine Results</b>	<b>35</b>
5.1 Optical Engine Test Conditions . . . . .	35
5.2 OH* Chemiluminescence . . . . .	36
5.2.1 Ignition Delay Time . . . . .	36
5.2.2 Flame Lift-off Length . . . . .	37
5.3 Light Extinction Measurements . . . . .	39
5.3.1 Spatial Soot Gradient in Quasi-Steady Period . . . . .	39
5.3.2 Temporal Soot Gradient in Premixed Combustion Phase . . . . .	41

<b>6 Discussion</b>	<b>45</b>
<b>7 Conclusions and Perspectives</b>	<b>49</b>
<b>A Fuel Analysis Sheets</b>	<b>51</b>
<b>B Optical Engine Results</b>	<b>57</b>
B.1 Tune Compression Ratio for In-Cylinder Gas Temperature Estimation .	57
B.2 Ignition Delay Time . . . . .	58
B.3 Flame Lift-off Length . . . . .	59
B.4 Spatial Soot Gradient . . . . .	60
B.5 Temporal Soot Gradient . . . . .	60
<b>Bibliography</b>	<b>61</b>

# List of Figures

1.1	Potential valorisation routes of glycerol [4, 5] . . . . .	1
2.1	Soot formation boundary conditions [11, 12] . . . . .	4
2.2	Quasi-steady combustion plume adapted from Dec[11] . . . . .	5
2.3	Biodiesel transesterification [22] . . . . .	9
3.1	Setup of the experimental investigation . . . . .	11
3.2	Emulsion preparation . . . . .	12
3.3	Instrumented Engine experimental setup . . . . .	15
3.4	Mechanical setup of the Optical Engine . . . . .	17
3.5	Compression ratio determination scheme . . . . .	18
3.6	Optical setup . . . . .	19
3.7	Camera exposure alignment . . . . .	20
3.8	Image lag characteristics . . . . .	22
3.9	Schematic light extinction measurement with an alternating light source	22
3.10	$KL$ saturation . . . . .	24
4.1	Ignition delay and combustion delay . . . . .	26
4.2	Ensemble of AHRR plots of the Instrumented Engine . . . . .	27
4.3	Brake thermal efficiency of the Instrumented Engine . . . . .	28
4.4	PM emissions Instrumented Engine - broad view . . . . .	29
4.5	Thermogravimetric analysis of exhaust particulate emissions . . . . .	30
4.6	PM emissions Instrumented Engine - detailed view . . . . .	31
4.7	CO & THC emissions . . . . .	32
4.8	NO <sub>x</sub> emissions . . . . .	33
5.1	Ignition delay time . . . . .	37
5.2	Determination of the instantaneous flame lift-off length . . . . .	38
5.3	Flame lift-off length . . . . .	38
5.4	Averaged OH* intensity over quasi-steady period . . . . .	39
5.5	Integrated $KL$ per pixel column during the quasi-steady phase . . . . .	40
5.6	Averaged $KL$ plots during the quasi-steady period . . . . .	41
5.7	Temporal development of the $KL$ during premixed phase . . . . .	42
5.8	Temporal development of the soot in the premixed phase . . . . .	43
6.1	TSG-IDT and SSG-FLOL correlation . . . . .	46
6.2	PM and CO brake specific emissions . . . . .	47
6.3	PM CO trade-off . . . . .	48
B.1	Ignition delay time - all results . . . . .	58
B.2	Flame lift-off length - all results . . . . .	59
B.3	Spatial soot gradient - all results . . . . .	60
B.4	Temporal soot gradient - all results . . . . .	60



# List of Tables

2.1	Fuel properties . . . . .	7
2.2	Previous studies on glycerol-diesel emulsions [6, 7, 28] . . . . .	10
3.1	Surfactant composition . . . . .	12
3.2	Fuel blend composition . . . . .	13
3.3	Fuel blend properties . . . . .	13
3.4	Instrumented Engine Properties . . . . .	14
4.1	Instrumented Engine operating parameters . . . . .	25
4.2	particulate matter filter samples . . . . .	30
5.1	Optical Engine operating parameters . . . . .	35
5.2	Optical Engine Condition Points . . . . .	36
5.3	Comparison of Injected Fuel Mass and Injected Energy . . . . .	36
5.4	Temporal Soot Gradient . . . . .	43
B.1	Calibration map for the Tuned Compression Ratio . . . . .	57



# List of Abbreviations

<b>AHRR</b>	Apparent Heat Release Rate
<b>BGs</b>	Background Static Level
<b>BSE</b>	Brake Specific Emissions
<b>BTE</b>	Brake Thermal Efficiency
<b>BW</b>	Bandwidth
<b>CA<sub>10</sub></b>	Crank Angle of 10 % Cumulative Heat Release
<b>CA<sub>50</sub></b>	Crank Angle of 50 % Cumulative Heat Release
<b>CAD</b>	Crank Angle Degree
<b>CN</b>	Cetane Number
<b>CR</b>	Compression Ratio
<b>DBIEI</b>	Diffuse Back-Illuminated Light Extinction Imaging
<b>DRef</b>	Reference Diesel
<b>ECU</b>	Engine Control Unit
<b>FLOL</b>	Flame Lift-off Length
<b>FWHM</b>	Full Width at Half Maximum
<b>G15</b>	15 w% Glycerol Diesel Emulsion
<b>HLB</b>	Hydrophilic-Lipophilic Balance
<b>IDT</b>	Ignition Delay Time
<b>LED</b>	Light-Emitting Diode
<b>LHV</b>	Lower Heating Value
<b>LPL</b>	Liquid Penetration Length
<b>NaN</b>	Not-a-Number
<b>PM</b>	Particulate Matter
<b>SOI</b>	Start of Injection
<b>SSG</b>	Spatial Soot Gradient
<b>T25</b>	25 w% TPGME Diesel Blend
<b>TDC</b>	Top Dead Center
<b>THC</b>	Total Unburned Hydrocarbons
<b>TPGME</b>	Tripropylene glycol monomethyl ether
<b>TSG</b>	Temporal Soot Gradient
<b>UV</b>	Ultraviolet





# List of Symbols

$A_{px}$	projected pixel area	[m <sup>2</sup> ]
$c_p$	specific heat at constant pressure	[kJ kg <sup>-1</sup> K <sup>-1</sup> ]
$c_v$	specific heat at constant volume	[kJ kg <sup>-1</sup> K <sup>-1</sup> ]
$d_p$	particle diameter	[nm]
$f_v$	volume fraction	[—]
$I_0$	initial light intensity	[W m <sup>-2</sup> ]
$I_0^*$	initial light intensity based on dark image	[W m <sup>-2</sup> ]
$I_B$	bright frame light intensity	[W m <sup>-2</sup> ]
$I_D$	dark frame light intensity	[W m <sup>-2</sup> ]
$I_f$	flame luminosity	[W m <sup>-2</sup> ]
$I_f^*$	flame luminosity based on dark image	[W m <sup>-2</sup> ]
$I_L$	image lag intensity	[W m <sup>-2</sup> ]
$I_t$	transmitted light intensity	[W m <sup>-2</sup> ]
$I_t^*$	transmitted light intensity based on dark image	[W m <sup>-2</sup> ]
$k_e$	non-dimensional extinction coefficient	[—]
$K$	dimensional extinction coefficient	[m <sup>-1</sup> ]
$L$	path length	[m]
$m$	in-cylinder mass	[kg]
$\dot{m}_{exhaust}$	exhaust mass flow	[kg s <sup>-1</sup> ]
$\dot{m}_{fuel}$	fuel consumption	[kg s <sup>-1</sup> ]
$\bar{m}_{inj}$	mean injected mass	[g]
$m_{soot}$	mass soot	[kg]
$MW$	molecular weight	[g mol <sup>-1</sup> ]
$n$	engine speed	[s <sup>-1</sup> ]
$n_m$	number of measurements	[—]
$N$	number of particles	[—]
$N_{inj}$	number of injections	[—]
$N_{rep}$	number of repeats	[—]
$p$	in-cylinder pressure	[bar]
$p_{in}$	inlet pressure	[bar]
$p_{TDC\ me.}$	measured pressure at TDC	[bar]
$p_{TDC\ mod.}$	modelled pressure at TDC	[bar]
$P_{out}$	generated power	[kW]
$Q_{ch}$	chemical heat release	[kJ]
$Q_{ht}$	heat transfer	[kJ]
$Q_n$	net heat release	[kJ]
$s$	standard deviation	[—]
$t$	time	[s]
$t_{95\%}$	95 % percentile of the $t$ distribution	[—]
$T$	in-cylinder temperature	[K]
$T_{dyno}$	torque dynamometer	[N m]
$T_{in}$	inlet temperature	[°C]

$T_{TDC\ mod.}$	modelled temperature at TDC	[K]
$V$	in-cylinder volume	[m <sup>3</sup> ]
$w$	weight	[kg]
$w_f$	weight fraction	[—]
$\bar{X}$	arithmetic average	[—]
$\alpha$	ratio positive image lag to intensity difference	[—]
$\beta$	ratio negative image lag to intensity difference	[—]
$\gamma$	ratio of specific heats	[—]
$\Phi$	equivalence ratio	[—]
$\lambda$	light wavelength	[m]
$\rho_{soot}$	soot density	[kg m <sup>-3</sup> ]
$\rho_{TDC\ mod.}$	modelled air density at TDC	[kg m <sup>-3</sup> ]
$\Omega$	oxygen ratio	[—]

## Chapter 1

# Introduction

Air pollution by internal combustion engines is a highly discussed issue which is most critical in cities. The European Union has set limits to several pollutants in ambient air where nitrogen oxide  $\text{NO}_x$  and particulate matter PM concentrations are within the most regarded [1]. As compression-ignited diesel engines are among the main emitters of these pollutants, their exhaust emissions are highly regulated and limits have been tightened in recent years [2, 3]. Although there are aftertreatment solutions to reduce nitrogen oxide and particulate matter emissions, there is a constant interest to reduce the cylinder-out emissions as aftertreatment is expensive and rarely complete.

Apart from pollutants directly harmful to human health, carbon dioxide  $\text{CO}_2$  emissions have to be reduced to counter climate change. This is why biodiesel usage has increased in the 2000s since the biomass-derived substitute has a reduced carbon footprint in comparison to fossil diesel. A by-product of biodiesel production is crude glycerol which has led to a surplus because traditional glycerol applications do not demand the increased amount. There are several investigations on how to add value to the redundant glycerol which focus on its utilisation in the fuel sector since a shortly closed product cycle is favoured due to economical and ecological reasons. Furthermore, the high oxygen content of glycerol is promising to have a soot reduction effect similar to what is observed for biodiesel. [4]

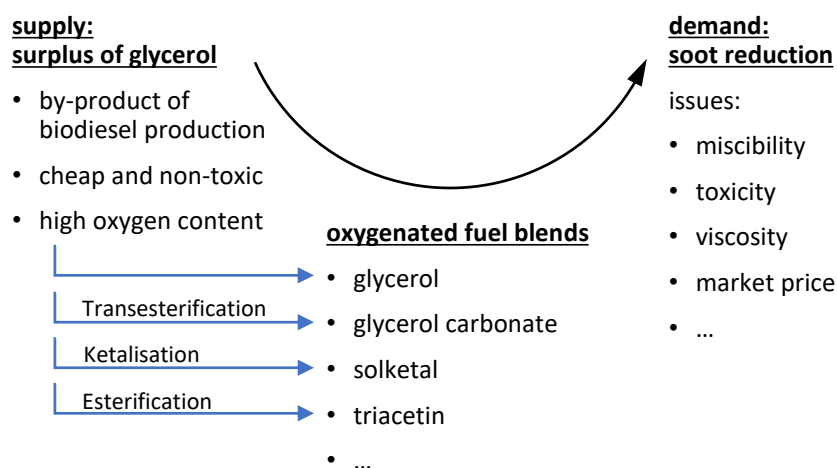


FIGURE 1.1: Potential valorisation routes of glycerol [4, 5]

This study is driven by two aspects. On one side, there is the supply of abundant glycerol which a value-added application has to be found for. On the other side, there is the demand for soot reducing fuel additives to meet future emission regulations. Thus, an oxygenated fuel blend based on glycerol could result in benefits in PM emissions and reduce of surplus of glycerol (see Figure 1.1). Recent studies have identified a diversity of possible candidates that can be produced from different chemical conversions [4, 5]. Most relevant issues for possible fuel blends are good miscibility with diesel, low toxicity, similar viscosity to diesel, and a low market price. Hereby, miscibility and viscosity generally worsen with increased oxygen content and the market price rises with the complexity of chemical conversions.

In this work, glycerol itself is investigated as a diesel fuel blend. The glycerol-diesel mixture is created as an emulsion with the addition of a surfactant, thereby keeping viscosity and miscibility in satisfactory levels. Further advantages of the direct use of purified glycerol are its non-toxicity, its high oxygen content, and omitting further chemical conversion. Previous studies on diesel engines have reported a smoke reduction when comparing glycerol-diesel emulsions to pure diesel [6, 7]. To the knowledge of the author, the detailed combustion behaviour is yet to be assessed. This is where the present study continues by providing a profound investigation of the combustion properties of a glycerol-diesel emulsion conducted in an instrumented six-cylinder engine and an optical accessible one-cylinder engine.

## Chapter 2

# Fundamentals

This chapter provides general information about glycerol as fuel and particulate matter formation in compression-ignition engines. Firstly, an overview of this pollutant, its formation, and relevant fuel parameters is given. Secondly, the fuel blend glycerol is presented, where its chemical properties are outlined and results of previous studies on its utilisation as a stand-alone fuel and as a fuel blend are summarised.

### 2.1 Soot Formation in Compression-Ignition Engines

Particulate matter PM and its carbonaceous solid fraction soot are a major concern since they are harmful to humans. The size of the particles is directly linked to their potential for causing health problems. As particles decrease in size, their reactivity and their ability to penetrate lower airways increases. Particles of enhanced health concern are "inhalable coarse particles" with a diameter range from 2.5 to 10  $\mu\text{m}$  and "fine particles" with less than 2.5  $\mu\text{m}$  in diameter. Epidemiological and experimental studies have demonstrated that exposure to particulate matter is linked to respiratory and cardiovascular diseases. [8]

Engine-out particulate matter consists principally of combustion generated soot on which organic compounds have become adsorbed [9]. Therefore, soot is regarded as a indicator of PM. Soot is a carbonaceous particle of highly complex geometry that results from incomplete combustion of fuel hydrocarbons, while some is contributed by the lubricating oil [9]. Its formation in combustion engines is the result of complex phenomena and can not be modelled precisely yet [10]. However, thermodynamic boundary conditions for soot formation are corroborated by several studies (see Figure 2.1) [11, 12].

Soot formation is located in the region of the fuel rich flame occurring at local equivalence ratios greater than  $\Phi > 2$  and temperatures higher than  $T > 1400$  K. Under these conditions injected fuel undergoes pyrolysis driving the formation of soot precursors, e.g., acetylene or polycyclic aromatic hydrocarbons. The precursors are involved in complex physico-chemical processes that lead to particle inception, called the nucleation mode. After their initial formation particles travel downstream and increase in size due to surface growth, coagulation and aggregation. Whenever particles reach regions of low equivalence ratios under high temperature conditions ( $T > 1350$  K), soot oxidation is taking place. The incompleteness of soot oxidation can be explained by particles being swept over the near stoichiometric combustion

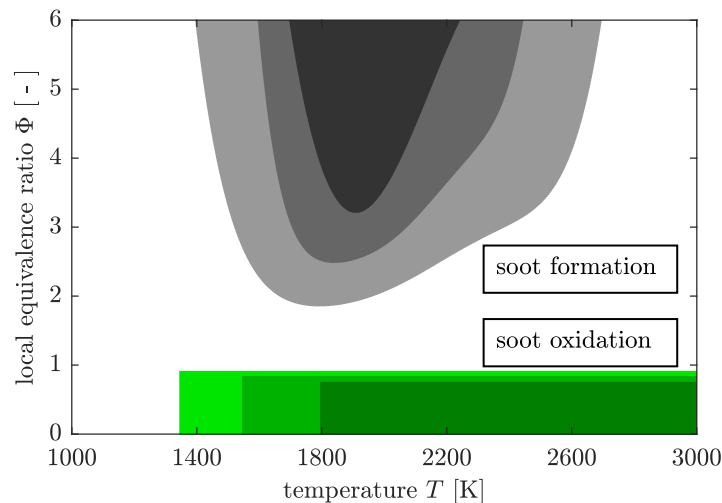


FIGURE 2.1: Thermodynamic boundary conditions for soot formation and oxidation adapted from Dec[11] and Pischinger[12]

zone and by ambient temperatures dropping under the oxidation level in the expansion stroke before all soot is oxidised. [9, 13]

To conclude, soot formation can be described as a result of a local lack of oxygen required for fuel oxidation. It can be influenced by mechanically dependent parameters (e.g., injection pressure, and in-cylinder swirl) and by fuel properties (e.g., oxygen content, and aromatic content). As the study targets at the combustion properties of different fuel compositions, mechanically dependent parameters are not investigated. In the following, the most important fuel properties and their effects on soot formation are presented. They are structured into fuel properties that affect soot formation due to chemical reaction characteristics and those that affect due to physical spray characteristics. Hereby, chemically-driven soot reduction is favoured because it is less dependent on engine specifications and operating conditions.

### 2.1.1 Chemically Effective Fuel Properties

#### Fuel Oxygen Content

Soot formation is chemically affected by the oxygen provided by the fuel. The fuel's inherent oxygen serves as oxidizer additionally to the air. Thus, a higher oxygen content reduces the local equivalence ratio and therefore lowers soot formation. This research field arose with biofuel production because these fuels consist of oxygenated hydrocarbons and proved to reduce soot emissions. To compare different oxygenated fuels regarding their oxygen content, Mueller et al. [14] introduced the oxygen ratio  $\Omega$ . It is defined as the molar ratio of the fuel's inherent oxygen and the total oxygen required for stoichiometric combustion. For a fuel consisting of only carbon, hydrogen, and oxygen, this ratio is simplified to the number of oxygen atoms in the fuel divided by half of the hydrogen atoms and twice the carbon atoms (see Equation 2.1).

$$\Omega = \frac{\text{oxygen provided by fuel}}{\text{oxygen required for stoichiometric combustion}} = \frac{n_{\text{O}}}{0.5 n_{\text{H}} + 2 n_{\text{C}}} \quad (2.1)$$

This parameter represents the percentage of oxygen required for combustion that is already covered by the fuel oxygen content. Unlike the oxygen weight or molar percentage, this parameter takes the fuel composition into account as hydrogen and carbon demand oxygen differently.

### Aromatic Content

Aromatic compounds are cyclic hydrocarbons that feature increased chemical stability due to a ring of resonance bonds. They are found to contribute to soot formation which can be linked to their lower reactivity and higher break-up resistance compared to non-aromatic compounds [9, 15]. Aromatic content is a commonly analysed fuel parameter.

### 2.1.2 Physically Effective Fuel Properties

Having a look at the physical parameters, diesel fuel combustion can be divided into a premixed phase and a quasi-steady phase. After the start of injection, fuel is mixing with air until the local equivalence ratio and the local temperature enable ignition. As soon as heat is released large parts of the fuel air mixture overcome the activation energy and burn, which is defined as the premixed combustion phase [9]. After this initial phase, the combustion stabilises as the continuously injected fuel requires mixing and heat transfer to form flammable fuel air mixtures. This phase is illustrated in Figure 2.2 and called the quasi-steady combustion period during which physical parameters can be assessed, e.g., the flame lift-off length FLOL, and the liquid penetration length LPL. In the following selected fuel parameters and their physical impact on soot formation are presented.

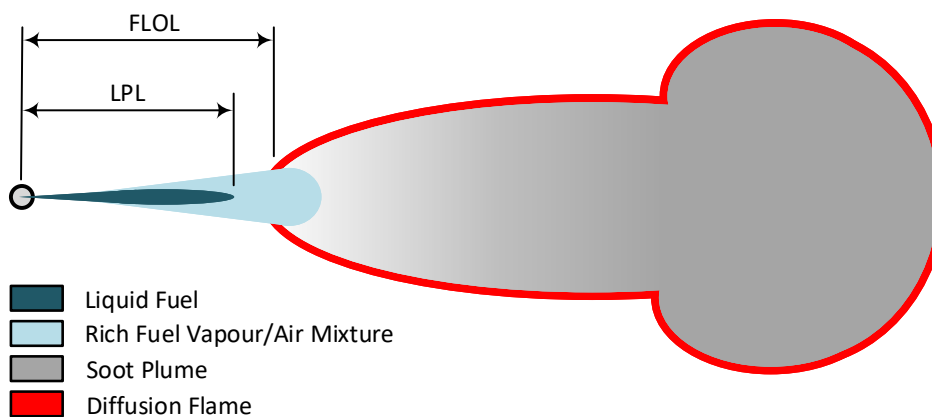


FIGURE 2.2: Quasi-steady combustion plume adapted from Dec[11]

### **Cetane Number & Flash Point**

The cetane number CN is the most common characteristic fuel number for diesel fuels and indicates the ignition delay. A high CN refers to a short ignition delay, i.e., a high fuel reactivity. Reijnders et al. [15] have elaborated that depending on the operating conditions a higher CN has resulted in both soot increase and soot reduction. As a high CN leads to a short ignition delay, less fuel air mixing time is provided. On the other hand, a high CN refers to a high fuel reactivity which reduces soot formation. In above cited study, a high cetane number is beneficial for soot reduction under high-temperature combustion conditions and has an increasingly negative effect with decreasing temperatures.

The flash point is defined as the lowest temperature where a substance is able to burn given an ignition source. The higher the flash point the less prone a fuel is to combust. The effect on soot formation of this parameter is similar to the CN with a low flash point indicating increased fuel reactivity but reduced fuel air mixing time.

Both parameters have physical effects on combustion properties. With the CN representing the ignition delay, it specifies the fuel air mixing time in the premixed combustion phase. The flash point affects the flame lift-off length which indicates the mixing time in the quasi-steady period. By observing the physical combustion parameters, effects on soot formation can be traced back.

In this study, the cetane number and the flash point are listed as physically effective properties. However, they are both physically and chemically effective as they also indicate fuel reactivity.

### **Boiling Point & Viscosity**

These two properties have an impact on spray characteristics. A common spray parameter is the liquid penetration length LPL which defines the length of the liquid spray in the quasi-steady combustion period (see Figure 2.2). If the boiling point is low, the fuel will vaporize earlier and show a shorter LPL. Assuming the FLOL would be constant, a shorter LPL contributes to soot reduction as fuel air mixing mechanisms are more effective in the gaseous phase.

A general effect of the viscosity on soot formation is not evaluated. However, the viscosity of a fuel blend should be similar to the reference fuel as the injector functionality is dependant on the viscosity.

### **Heating Value**

The heating value is the most important parameter for a fuel describing the amount of energy that can theoretically be extracted per mass. Diesel engines operate within a range of heating value, therefore low-calorific fuel blends can only be added in limited percentages. Soot formation is indirectly affected by the heating value due to changes in the total mass of fuel injected, therefore changes in injection duration, injection pressure, and injection timing may be required.



## 2.2 Glycerol as a Fuel

In the beginning of the century, biodiesel production has increased rapidly because its CO<sub>2</sub> footprint is reduced compared to fossil diesel [4]. This has led to a surplus of its by-product glycerol and set the interest to add value to it. Despite some challenging properties of glycerol, studies have proven that stable glycerol combustion is possible and that its utilisation as a fuel blend in internal combustion engines can have positive effects on its emissions [6, 7].

### 2.2.1 Glycerol General Information

Glycerol is an organic compound with the chemical formula C<sub>3</sub>H<sub>8</sub>O<sub>3</sub>. It is a low toxicity alcohol that consists of a three-carbon chain with a hydroxyl group attached to each carbon. These groups are responsible for glycerol being hygroscopic and water-soluble. Glycerol has low volatility and low vapour pressure and is non-toxic to both humans and the environment. Physically, glycerol is a clear, colourless, odourless, viscous and sweet-tasting liquid [4]. Traditional uses of glycerol are pharmaceutical, personal care, and food products, but they cannot absorb the increase due to biodiesel production.

TABLE 2.1: Fuel properties

Property	Unit	Reference Diesel	Glycerol	TPGME
chemical formula		C <sub>11–14</sub> H <sub>22–28</sub> <sup>b</sup>	C <sub>3</sub> H <sub>8</sub> O <sub>3</sub>	C <sub>10</sub> H <sub>22</sub> O <sub>4</sub>
oxygen ratio <sup>j</sup>	[ % ]	0.0	30.0	12.9
molecular weight	[g/mol]	176.2 <sup>b</sup>	92.09	206.3
specific gravity	[g/ml]	0.823 <sup>a</sup>	1.26 <sup>c</sup>	0.963 <sup>h</sup>
kinematic viscosity	[cSt]	2.53 <sup>a</sup>	270 <sup>d</sup>	4.1 <sup>d</sup>
lower heating value	[MJ/kg]	43.33 <sup>a</sup>	16.06 <sup>e</sup>	27.7 <sup>h</sup>
cetane number		60.4 <sup>a</sup>	5 <sup>f</sup>	65 <sup>h</sup>
initial boiling point	[°C]	212 <sup>a</sup>	290 <sup>g</sup>	243 <sup>i</sup>
flash point	[°C]	90.5 <sup>a</sup>	177 <sup>g</sup>	121 <sup>i</sup>

a: reference diesel analysis (see Appendix A); b: derived from reference diesel analysis; c: glycerol analysis (see Appendix A); d: measured; e: based on standard formation enthalpy [16]; f: according to Setyawan et al. [17]; g: according to Sidhu et al. [7]; h: determined by Dumitrescu et al. [18]; i: according to PubChem [19]; j: defined by Mueller et al. [14]

Comparing the properties of glycerol to the reference diesel, three main challenges regarding its utilisation as a diesel fuel blend can be deduced: its miscibility with diesel, its viscosity, and its ignitability. Glycerol and fossil diesel are immiscible which can be traced back to the polar hydroxyl groups of glycerol. Additionally to the polarity, the difference in density enhances a separation process. Secondly, the viscosity of glycerol is very high in comparison to the reference diesel, which affects the functionality of the injection system. Thirdly and arguably the most significant, glycerol is hard to ignite, which is indicated by the flash point and the cetane number. Table 2.1 also shows that glycerol has a high boiling point which contributes to

delayed vaporisation, i.e., delayed formation of flammable fuel air mixtures. Furthermore, the heating value of glycerol is less than half of the diesel providing less power per injected mass. By using glycerol as a fuel blend, it is assumed that the poor ignition properties of glycerol are absorbed by the diesel.

Another known issue of glycerol combustion is the formation of toxic acrolein, which is a product of its thermal decomposition when heated between 280 and 300 °C, well below glycerol's self-ignition temperature. Acrolein is toxic in very small quantities, around 2 ppm. Acrolein is increasingly unstable at high temperatures and highly flammable, totally consumed between 930 and 1000 °C. It's conceivable that an efficient glycerol flame could consume any acrolein produced before combustion gases are released in the environment [20]. However, acrolein measurements are currently not part of standardised gaseous emission analysers, which is why this issue is kept in mind but can not be investigated in this study.

Promising properties of glycerol are its non-toxicity to humans and the environment as well as its high oxygen content. With an oxygen ratio of 30 %, pure glycerol provides a third of the oxygen required for stoichiometric combustion on its own. Thus, it is expected to decrease the local equivalence ratio and consequently reduce soot formation if used as a fuel blend.

To improve the comparability, tripropylene glycol monomethyl ether TPGME is investigated as a benchmark soot reducing fuel blend. TPGME has proven to lower soot formation in previous studies by Manin et al. [21] and Dumitrescu et al. [18]. Regarding its properties, it shows fewer differences to the reference diesel than glycerol (see Table 2.1).

## 2.2.2 Glycerol as a By-Product of Biodiesel Production

As the motivation to use glycerol as a fuel blend is highly related to biodiesel production, a summary of the process is given. The most common method to produce biodiesel from vegetable oils or animal fats is transesterification where an alcohol is displaced from an ester by another. The feedstock triacylglycerides reacts with a short chain alcohol (most commonly methanol) under the presence of an alkaline catalyst and forms alkyl esters and glycerol (see Figure 2.3). The alkyl esters are separated from the crude glycerol by phase separation and are refined to meet biodiesel fuel specifications. Non-reacted alcohols and the catalyst are partly removed from the crude glycerol and recycled, leading to a by-product quality of approximately 85 % glycerol with contaminations of methanol, water and corrosive salts [22, 23]. In this study, purified glycerol is investigated to determine whether glycerol is a beneficial fuel blend and to rule out any effects of contamination.

## 2.2.3 Pure Glycerol Combustion

One way to add value to the surplus of glycerol is its utilization as a stand-alone fuel. The majority of these investigations focus on crude glycerol combustion as a boiler fuel. Studies on a burner by Steinmetz et al. [24] show that the challenges related to flame ignition and stability can be overcome by using a high swirl burner. However, large particulate mass emissions are observed which are considered to be caused by soluble catalysts left over from biodiesel production.

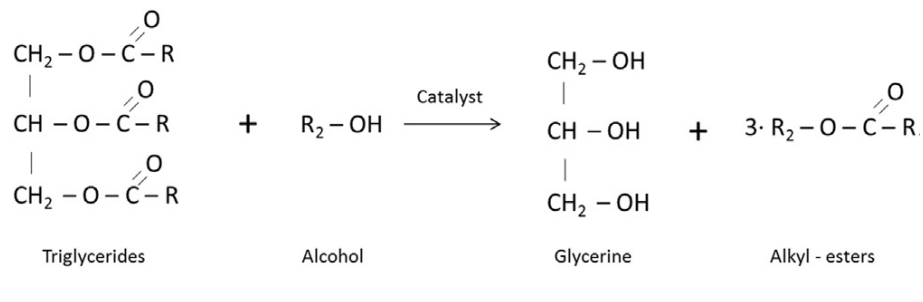


FIGURE 2.3: Biodiesel transesterification [22]

McNeil et al. [25] have tested a two-cylinder naturally aspirated Lister Petter diesel engine fuelled with purified glycerol. After an engine warm-up on fossil diesel, the fuel is switched to glycerol. The inlet air temperature is varied and the effect on the combustion is investigated. It is found that the optimal inlet air temperature for this engine is 144 °C, while glycerol combustion completely failed with an inlet temperature below 90 °C. Comparing the exhaust gas emissions to fossil diesel, an increase in carbon monoxide and a decrease in NO<sub>x</sub> is observed. Furthermore, a compatibility issue with the lubricating oil is reported. Based on these studies diesel generators running on purified glycerol provide electric power for the Formula E events [26].

#### 2.2.4 Glycerol Diesel Emulsions

An emulsion is a thermodynamically metastable mixture of two or more immiscible liquids where one liquid is dispersed in the other. The investigated glycerol-diesel emulsions form a water-in-oil like emulsion with glycerol droplets being dispersed in a continuous diesel phase. Over time, the glycerol droplets sink to the bottom and coalesce. The stability of the emulsion increases with finer dispersed droplets and the addition of a surfactant that stabilizes the phase interface. Surfactants consist of hydrophilic and lipophilic groups that interact with both liquids. The hydrophilic-lipophilic balance HLB specifies whether a surfactant is rather oil-loving (HLB = 0) or water-loving (HLB = 18) and can also be tuned by mixing two surfactants. [6, 27]

Eaton et al. [6] were first to investigate glycerol-diesel fuel emulsions in 2014. They conducted a surfactant screening with a total of eight surfactants examining interfacial surface tension and concluded that a mixture of Tween 80 and Span 80 yields optimal stability. In a second step, long-term stability of glycerol diesel emulsions was investigated using previously chosen surfactants with various HLB values and concentrations. Hereby, the stability was monitored under isothermal conditions until full phase separation was observed. It is reported that sedimentation ranged between 10 and 100 h and the earliest complete separation occurred after 42 h. Based on the stability results, a 10 vol% and a 20 vol% glycerol diesel emulsion was prepared using a surfactant mixture of Span 80 and Tween 80 (HLB = 6) at a concentration of 1 vol%. The emulsion was created in 200 ml continuously stirred batches with an ultrasonic processor outputting 1600 J at a rate of 45 W. [6]

Ultimately, the combustion behaviour was evaluated on a naturally aspired, single-cylinder engine (see Table 2.2). Increasing glycerol amount was found to retard combustion. Brake specific exhaust emissions have shown a smoke reduction at

high loads and an increase of carbon monoxide CO and total unburned hydrocarbons THC at low loads. Furthermore, increased brake thermal efficiency is observed when using the 10 vol% glycerol-diesel emulsion. [6]

In 2019, Eaton et al. [28] repeated the investigation on a medium-speed diesel engine measuring PM emissions with a particle number size spectrometer. Effects on the ignition delay, efficiency, and gaseous emissions were consistent with their previous study, however a reduction in PM could not be confirmed observing only a shift to smaller particles.

TABLE 2.2: Previous studies on glycerol-diesel emulsions [6, 7, 28]

Author Year	Eaton et al. [6] 2014	Sidhu et al. [7] 2018	Eaton et al. [28] 2019
Engine Displacement	Hatz 1D50z 517 cm <sup>3</sup>	Hatz 2G40 997 cm <sup>3</sup>	Wärtsilä 6L20 8.8 l
Emulsification Surfactant	ultrasonic treatment Span 80 & Tween 80	high-shear force blender Span 80 & Tween 80	resonant homogeniser n.d.
PM Equipment PM Emission	smoke opacity meter reduction at high loads	smoke opacity meter reduction at all loads	number size spectrometer shift to smaller particles

A similar study with a greater amount of engine conditions was conducted by Sidhu et al. [7] in 2018. In contrast to the previous studies, glycerol was produced from an on-site laboratory-scale biodiesel production with glycerol purification. The emulsion was created using a high-shear force blender and a surfactant mixture of Span 80 and Tween 80 with HLB = 6.4. Among other fuel mixtures pure diesel, a 5 w% glycerol-diesel emulsion and a 10 w% glycerol-diesel emulsion were investigated. Viscosity measurements have shown that by using glycerol in the form of an emulsion the issue its very high viscosity can be avoided.

Emissions and combustion efficiency were examined on a two-cylinder, four-stroke diesel engine (see Table 2.2). The addition of glycerol resulted in increased carbon monoxide and unburned hydrocarbon emissions as similarly reported by previous studies [6, 25]. However, smoke opacity measurements have shown significantly decreased levels with increasing glycerol concentration, a trend that was consistent across all investigated engine loads and speeds. Additionally, nitrogen oxide emissions could be reduced and increased brake-thermal efficiency is observed with the addition of glycerol.

In conclusion, the studies on glycerol-diesel emulsions have shown beneficial effects regarding smoke emissions and efficiency on specific engines. To continue the investigation, the present study focuses on the further assessment of the combustion behaviour to evaluate if glycerol is a beneficial fuel blend in general.

## Chapter 3

# Experimental Setup

The experimental setup consists of two independent test rigs, an instrumented six-cylinder engine and an optical accessible one-cylinder engine. The Instrumented Engine is equipped with exhaust gas and particulate matter analysis and is used to examine global parameters like emissions and specific fuel consumption (see Figure 3.1). The Optical Engine is a modified one-cylinder engine with two high-speed cameras mounted that capture light extinction and OH\* chemiluminescence. Thereby, detailed combustion parameters (e.g., flame lift-off length) and in-flame soot formation can be determined. This chapter presents the fuel preparation and the experimental setup of both test rigs.

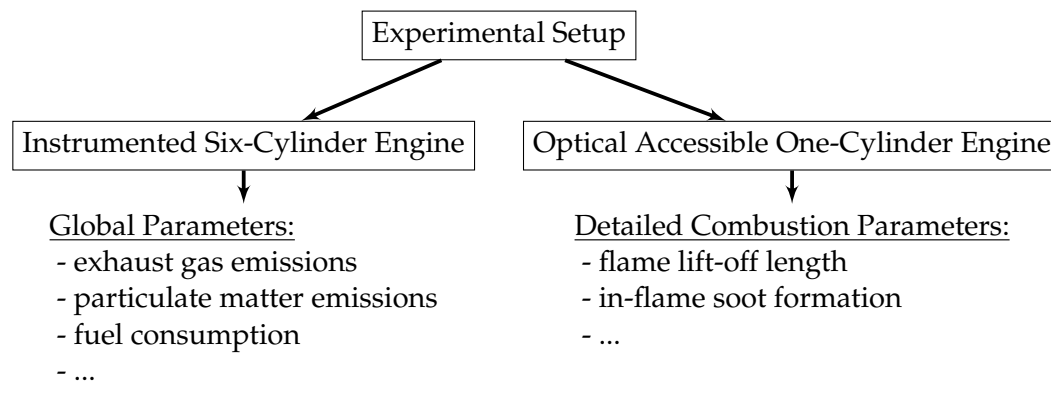


FIGURE 3.1: Setup of the experimental investigation

## 3.1 Fuel Preparation

The combustion behaviour of the glycerol emulsion is assessed in comparison to pure reference diesel. In the Optical Engine, it is additionally compared to a TPGME-diesel mixture. As the characteristics of an emulsion depend on its preparation process, it is described next. Secondly, the composition of the investigated fuels and its characteristic fuel numbers are presented.

### 3.1.1 Emulsion Preparation

As glycerol and diesel repel each other, a surfactant (surface active agent) is needed to achieve a homogeneous mixture. The surfactant selection is based on a screening

TABLE 3.1: Surfactant composition

	Span 80	Tween 80
full name	Sorbitan monooleate	Polyoxyethylene-sorbitan monooleate
linear formula	$C_{24}H_{44}O_6$	$C_{64}H_{124}O_{26}$
weight percentage	80 %	20 %
HLB	4.3	15

conducted by Eaton et al. [6]. A mixture of two widely used surfactants known as Span 80 and Tween 80 with a lipophilic-hydrophilic balance of HLB = 6.4 was chosen (see Table 3.1). It was prepared prior to the emulsion by stirring the two highly viscous liquids until a homogeneous fluid was obtained. The same surfactant as in previous studies [6, 7] was not only chosen because it has already shown good results but also to keep the comparability between this study and previous studies high.

The emulsion was prepared by mixing the surfactant mixture and glycerol first. They were blended using a magnetic stirrer for 5 to 15 minutes depending on the amount of mixture until no colour gradients were detectable. Subsequently, the diesel was added and the mixture was stirred for additional 15 minutes.

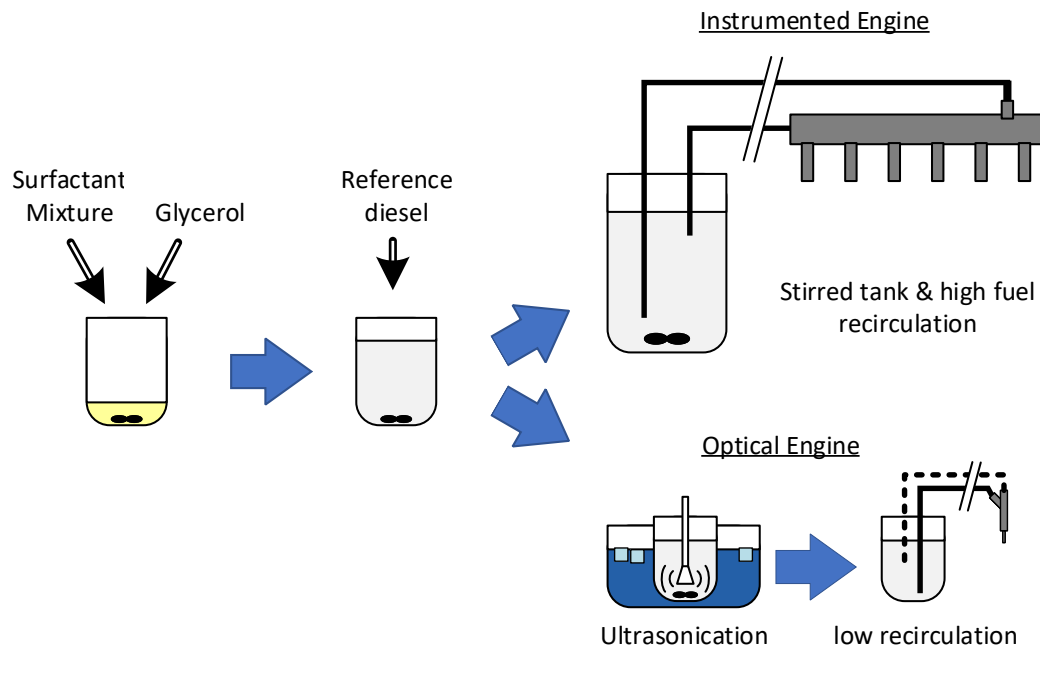


FIGURE 3.2: Emulsion preparation

For the Instrumented Engine, an amount of 12 l was prepared in 4 l batches and the emulsion was kept being stirred in the tank during the experiments (see Figure 3.2). An ultrasonic treatment could not be realized due to the high amount. With the fuel return from the common rail being led back into the tank, fuel recirculation was high. It is observed that the fuel pressure pump contributes to emulsion stability which is interpreted as a cause of high-shear forces in the pump.

For investigations in the Optical Engine, a fuel amount of only 300 ml was needed, but there was little fuel recirculation in the system. To counter the long residence time in the fuel system before being injected, the emulsion was treated with ultrasonication to further decrease droplet size and increase emulsion stability [27]. A handheld ultrasonic homogenizer Hielscher UP200Ht was used for a period of 5 minutes at a rate of 200 W. To minimize fuel heating, the mixture was placed in an ice bath (see Figure 3.2).

### 3.1.2 Fuel Composition

The experimental investigation was conducted with a reference diesel fuel that complies with the European standard for automotive diesel, EN 590. In order to evaluate the effect of the glycerol, the pure reference diesel (DRef) was examined first. It was then compared to a 15 w% glycerol fuel blend, further referred to as G15. The surfactant mixture was added in a 1:10 volumetric ratio to the glycerol content resulting in a weight percentage of 1.14 w%.

In the Optical Engine, a 25 w% TPGME-diesel fuel blend (T25) was investigated as an additional benchmark. Hereby, the content of TPGME was chosen to match the oxygen ratio of the G15 (see Table 3.3). The exact composition of all fuels is shown in Table 3.2, while an analysis of all feedstock fuels is provided in Appendix A.

TABLE 3.2: Fuel blend composition

Component	Unit	DRef	G15	T25
Reference Diesel	[w%]	100.0	84.60	75.14
Glycerol	[w%]	0.0	14.26	0.00
Surfactant Mixture	[w%]	0.0	1.14	0.00
TPGME	[w%]	0.0	0.00	24.86

The glycerol content was selected with regard to the properties of biodiesel which has an oxygen ratio of approximately  $\Omega = 3.7\%$  and a LHV of 37.8 MJ/kg [29]. The G15 features a heating value and an oxygen ratio comparable to a 70 % biodiesel blend. Therefore, it is expected to show noticeable differences compared to pure diesel. On the other hand, the glycerol concentration was opted to be as low as possible in order to ensure functional combustion conditions given the glycerol's poor ignitability.

TABLE 3.3: Fuel blend properties

Property	Unit	DRef	G15	T25
specific gravity	[g/ml]	0.823 <sup>a</sup>	0.867 <sup>b</sup>	0.854 <sup>b</sup>
kinematic viscosity	[cSt]	2.534 <sup>a</sup>	3.55 <sup>c</sup>	2.90 <sup>c</sup>
lower heating value	[MJ/kg]	43.33 <sup>a</sup>	39.40	39.44
oxygen ratio <sup>d</sup>	[%]	0.00	2.46	2.46
molar O/C ratio	[%]	0.00	7.22	7.23

a: reference diesel analysis (see Appendix A); b: estimated; c: measured; d: defined by Mueller et al. [14]

Fuel properties of the selected fuel compositions are presented in Table 3.3. Viscosity measurements have proven that satisfactory levels are achieved by using glycerol in form of an emulsion. The comparison between the G15 and the T25 illustrates that both fuel blends have very similar properties.

### 3.2 Instrumented Six-Cylinder Engine

The Instrumented Engine consists of a six-cylinder diesel engine that is equipped with a PM analyser, a gaseous emissions analyser, and several pressure and temperature measurements. It is set up to examine engine efficiency and emissions in conditions close to automotive application. Exhaust gas recirculation, oxidation catalyst and particulate matter filter are removed in order to determine the raw cylinder-out emissions.

TABLE 3.4: Instrumented Engine Properties

Engine Parameter	Specification
type	straight six-cylinder, four-stroke, turbo-charged
model	Mercedes OM613
displaced volume	3222 ml
bore / stroke	80 mm / 88.3 mm
compression ratio	18:1
engine torque	470 Nm at 1800 - 2600 rpm
emissions analyser	DMS500 MkII & Horiba MEXA-ONE-RS

The engine is a straight six-cylinder, turbo-charged diesel engine with a displacement of 3.2 litres and common rail fuel injection (see Table 3.4). The engine torque is countervailed by a water dynamometer, which is limited to 140 Nm at the speed used and thereby defines the maximal engine load condition (see Section 4.1). During experiments, the engine torque is constantly measured using a Totalcomp TS-1.5K force transmitter.

The whole engine setup is illustrated in Figure 3.3. Fuel is injected as a single injection using the engine's original equipment. Redundant fuel from the common rail passes through a heat exchanger and returns into the fuel tank, which is placed on scales to measure fuel consumption. The fuel temperature before the fuel pressure pump is constantly observed during experiments. The air mass flow is measured using an orifice plate at the inlet. Furthermore, the turbocharger speed and the boost pressure are recorded. Engine parameters are set with the ECU-software Modas Sport, where engine speed is controlled automatically by adjusting the injection duration, whereas start of injection, turbocharge and injection pressure are set manually.

To determine combustion behaviour, cylinder one is equipped with a high-speed Kistler 6052C pressure sensor. A magnetic shaft encoder with 3200 readings per revolution tracks the crankshaft position resulting in a resolution of 0.11 crank angle degree per signal. Emission measurements are divided into PM and gaseous emissions. Both are sampled simultaneously at the same location downstream the exhaust pipe.



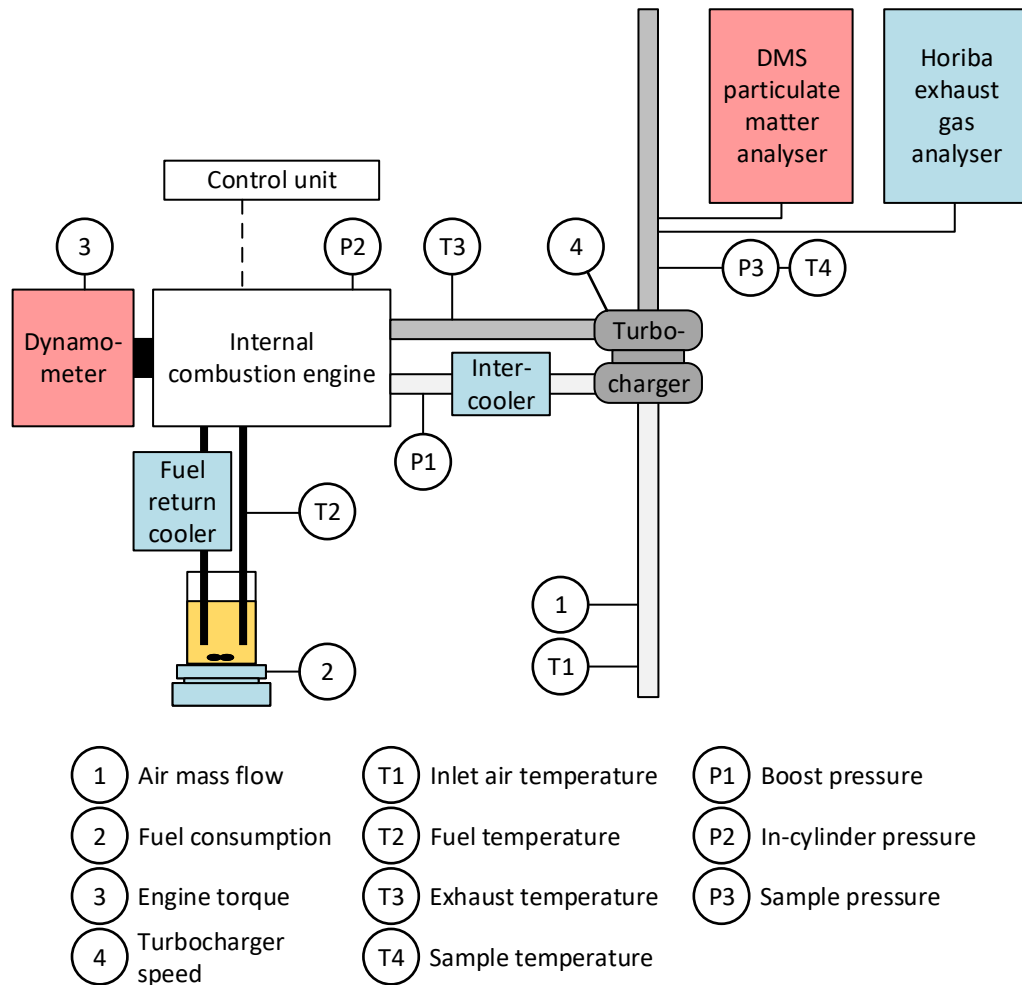


FIGURE 3.3: Instrumented Engine experimental setup

PM emissions are determined using a DMS500 MkII fast particulate spectrometer, which features a particle size measurement range of 5 nm to 1  $\mu\text{m}$ . Particles are charged electrically and drift through a radial electrical field thereafter. Depending on their aerodynamic drag/charge ratio, particles are detected at different distances on the in total 22 electrometers [30].

A Horiba Gas Analyser MEXA-ONE-RS records the exhaust gas composition. Measurements include carbon monoxide CO by non-dispersive infrared, total unburned hydrocarbons THC by flame ionization, as well as nitrogen monoxide NO and total nitrogen oxide  $\text{NO}_x$  by chemiluminescence.

### Methods Instrumented Engine

In-cylinder pressure is a common measurement, from which other information about the combustion behaviour can be derived. Based on the first thermodynamic law for an open, quasi-static system, energy transfer can be described by Equation 3.1.

Hereby, the net heat release  $Q_n$  includes the chemical energy  $Q_{ch}$  and the heat transfer to the environment  $Q_{ht}$ . The sensible enthalpy of the injected fuel and crevice flow are neglected. [9]

$$\frac{dQ_n}{dt} = \frac{dQ_{ch}}{dt} - \frac{dQ_{ht}}{dt} = mc_v \frac{dT}{dt} + p \frac{dV}{dt} \quad (3.1)$$

Applying the ideal gas law to Equation 3.1, the net heat-release becomes a function of in-cylinder pressure  $p$ , cylinder volume  $V$ , and the ratio of specific heats  $\gamma = c_p/c_v$  (see Equation 3.2). Hereby, cylinder volume is a function of crank angle degree. Thus, the temporally derived net heat release, further referred to as the apparent heat release rate AHRR, can be determined by the crank-angle-resolved pressure measurement. It is commonly interpreted as the released chemical energy because the heat transfer to the environment is quantitatively lower. [9]

$$\frac{dQ_n}{dt} = \frac{\gamma}{\gamma-1} p \frac{dV}{dt} + \frac{1}{\gamma-1} V \frac{dp}{dt} \quad (3.2)$$

Based on the apparent heat release rate, further parameters can be derived, e.g., the cumulative heat release, crank angle degree of 50 % cumulative heat release  $CA_{50}$ , and crank angle degree of 10 % cumulative heat release  $CA_{10}$ . Latter is commonly used as the start of ignition.

### 3.3 Optical Accessible One-Cylinder Engine

The Optical Engine is a single-cylinder engine with a modified head to allow optical access for profound investigation of combustion parameters. More detailed information about the experimental setup and the measuring techniques is provided in this section. Firstly, the mechanical setup and the estimation of the in-cylinder conditions are presented. Secondly, the applied optical methods are introduced and the optical setup is illustrated. Thirdly, non-ideal camera characteristics and their handling are covered.

#### 3.3.1 Mechanical Setup

The Optical Engine is a redesigned four-stroke, single-cylinder Lister 12 CS engine with a displacement of 1.85 litres and a geometric compression ratio of 15.9. It is driven by a 161 kW electric drive that maintains constant engine speed during the whole engine cycle, thereby allowing investigation independent from the torque generated by combustion. The engine's original crankcase and crankshaft are used. The crankshaft position is tracked by a magnetic shaft encoder with 3200 readings per revolution, giving a resolution of 0.11 crank angle degree per signal. A dynamic pressure sensor (Kistler 6052C) is installed to collect motored and combustion pressure cycles.

Figure 3.4 illustrates the mechanical setup. The inlet conditions are set using an air compressor and a 2 kW electric flow heater. Inlet air pressure can be varied from 1.0 bar to 1.55 bar, inlet air temperature from 55 °C to 135 °C. Fuel is pressurised by a compressed air-driven pressure pump and injected using a Bosch solenoid injector

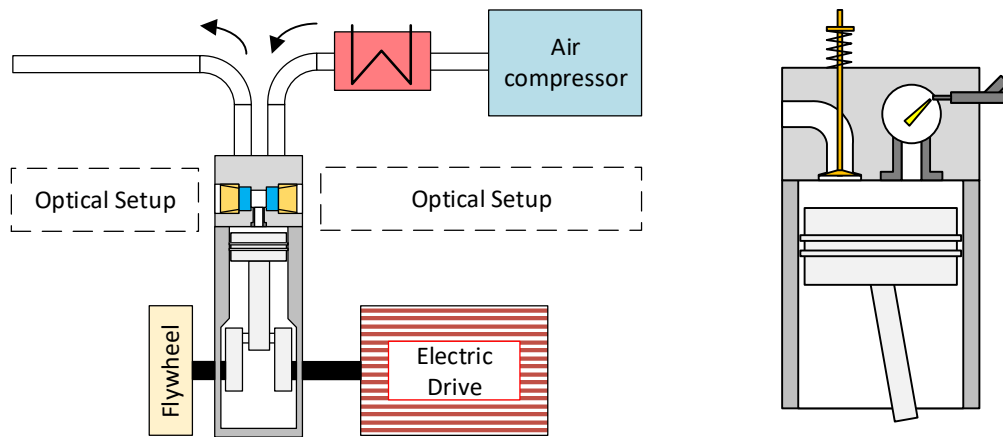


FIGURE 3.4: left: mechanical setup of the Optical Engine; right: vertical section view through the cylinder head

equipped with a modified nozzle (Bosch DSLA124P1659) with a single hole. Data acquisition, temperature control, tracking of crank position, injection triggering, and triggering of the optical measurements are controlled using the software LabVIEW.

The engine's head is modified to provide horizontal optical access (see Figure 3.4). It consists of a combustion chamber with cylindrical shape, 50 mm in diameter and 40 mm in depth, sealed with two quartz glass windows, 25 mm thick and 63 mm in diameter. The windows are retained by conically shaped bronze rings in order to maximize the angular access. The swept volume and the chamber are connected via an interchangeable throat. For this study, the throat that introduced the least swirl into the chamber was installed. The head uses the original intake and exhaust valves.

### 3.3.2 Estimation of In-Cylinder Conditions

While in-cylinder pressure is measured during experiments, in-cylinder temperature can only be estimated. A common approach to determine the gas temperature in internal combustion engines is to apply ideal gas law and derive the temperature from the pressure measurement and crankshaft encoding given a known engine geometry. On the other hand, in-cylinder gas parameters can also be modelled based on the engine dimensions and a heat transfer model. However, measured and predicted pressures in the Optical Engine did not match for motored pressure cycles, which is assumed to be caused by a significant air mass blow-by. As blow-by is a difficult quantity to determine, it is accounted for by decreasing the compression ratio in the model as shown in Figure 3.5.

Starting with the real engine dimensions, motored pressure cycles are predicted with a zero-dimensional model, which is based on energy conservation, ideal gas law, Woschni heat transfer correlation [31], and temperature dependent gas properties applying NASA polynomials [32]. Predicted and measured pressures are compared thereafter, adjusting the compression ratio until they match at TDC. The compression ratio is tuned by varying the clearance volume whereas the displaced volume is kept constant. This procedure was repeated for 12 cases across the inlet conditions

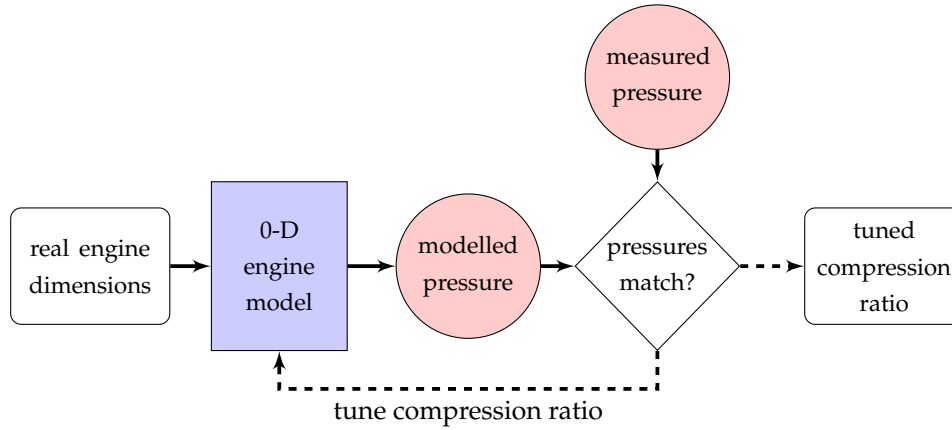


FIGURE 3.5: Compression ratio determination scheme to match predicted and measured pressures

and resulted in a tuned compression ratio of 12.43 (geometric CR = 15.9) with a maximal deviation of  $\pm 0.03$ . The whole test map is illustrated in Appendix B.1. The consistency of these results across the operating conditions confirms that this approach yields comparable gas temperature estimations. Based on this tuned compression ratio, the investigated conditions in the Optical Engine are chosen (see Section 5.1).

### 3.3.3 Optical Methods

The optical setup utilises the optical techniques Diffuse Back-Illuminated Light Extinction Imaging (DBIEI) and OH\* Chemiluminescence Imaging, which will be described briefly in this section.

DBIEI is a two-dimensional measurement of light intensity which is reduced due to scattering and absorption from particles present in the light path. From the ratio between the transmitted intensity  $I_t$  and the original light intensity  $I_0$ , the product of the dimensional extinction coefficient  $K$  and the path length  $L$  can be determined based on the Beer-Lambert law (see Equation 3.3) [33].

$$\frac{I_t}{I_0} = e^{-KL} \quad (3.3)$$

The dimensional extinction coefficient  $K$  can be related to a soot volume fraction. Assuming that the collection cone of the optical setup is small, the gas volume represented by a pixel is the product of the path length  $L$  and the projected pixel area  $A_{px}$ . Thus, the soot mass present in a pixel's light path can be described by Equation 3.4, which shows a proportional dependency of  $KL$  and the present soot mass [34].

$$m_{soot,px} = \rho_{soot} \frac{\lambda}{k_e} A_{px} KL \quad (3.4)$$

Hereby,  $\rho_{soot}$  is the soot density,  $\lambda$  is the wavelength of the light source and  $k_e$  is the non-dimensional extinction coefficient. In this study, a soot density  $\rho_{soot}$  of  $1.8 \text{ g/cm}^3$  and an extinction coefficient of  $k_e = 7.2$  are implemented according to the recommendation of Skeen et al. [34] for a 623 nm wavelength light source. Applying the

present LED wavelength ( $\lambda = 628 \text{ nm}$ ) and pixel resolution ( $0.163 \text{ mm/px}$ ) results in a conversion factor of  $4.171 \cdot 10^{-3} \mu\text{g}_{\text{soot}}/KL$ .

OH\* Chemiluminescence describes the phenomenon of natural flame luminosity in the UV wavelength range of 310 nm from short-lived excited-state OH\* radicals. They indicate high temperature and stoichiometric combustion conditions in the flame [35]. High-speed imaging of this instantaneous luminosity provides information about when and where high temperature combustion starts, which can be used to determine the flame lift-off length and the ignition delay time. As soot formation is sensitive to the air fuel mixing process prior to combustion, this measurement provides further information on whether soot formation is influenced by reaction kinetics or by physical mixing characteristics (see Section 2.1).

### 3.3.4 Optical Setup

The optical setup consists of a light source side and a collection side (see Figure 3.6). The aim of the light source side is to ensure that the light input to the chamber is collimated and uniformly distributed. A square SST-90-R LED from Luminus Devices Inc. provides a red light source at 628 nm wavelength (FWHM 15 nm). The LED is pulsed at 50 kHz for a duration of  $1.33 \mu\text{s}$  with the driver voltage being set to 30 V. The light pulse is measured with a photodiode and aligned with the camera exposure in such way that the camera is exposed to as much light as possible.

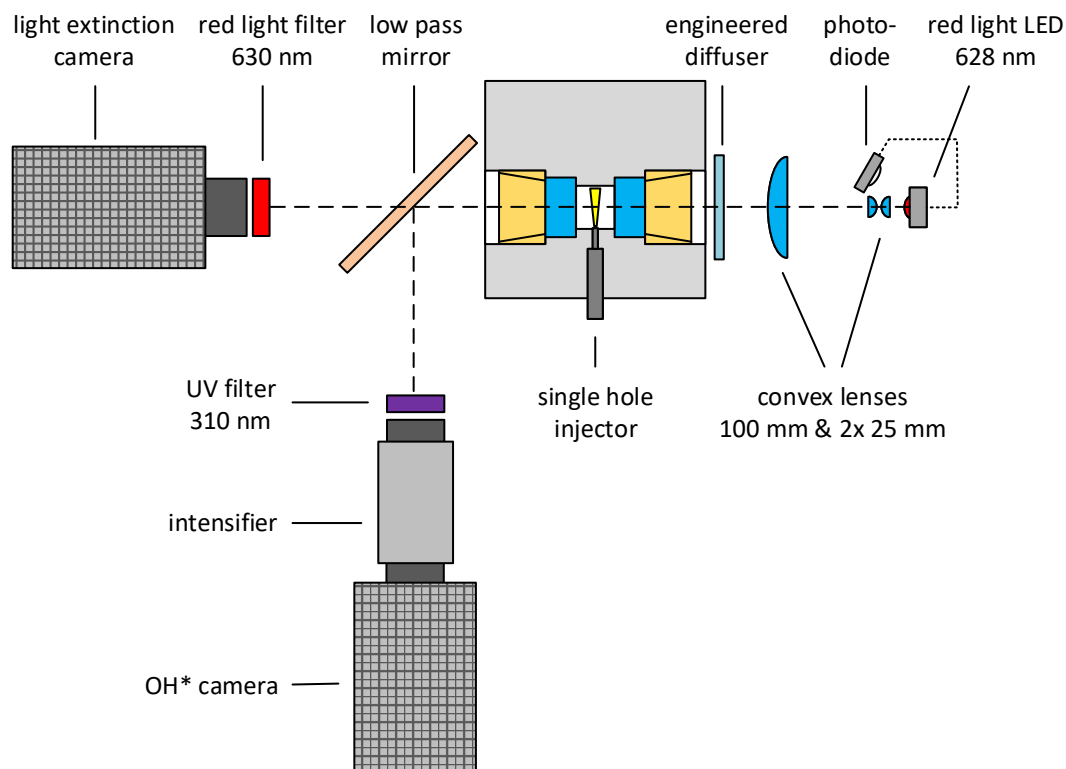


FIGURE 3.6: Optical setup

In front of the LED, two identical 25 mm diameter aspheric condenser lenses (Thorlabs ACL25416U-A) oriented in opposite position to each other are used to gather

and focus the light onto a collimating lens with 100 mm in diameter and a focal length of 100 mm. Before entering the chamber, the light beam passes an engineered diffuser with a full divergence angle of 15 degrees (RPC Photonics EDC-15-15132-A). More detailed information about the setup of the light source side can be obtained from the study of Bjørgen et al. [36].

Diffuse back-illuminated extinction imaging generally suffers from beam steering due to high density gradients, but effects can be minimized by adjusting the setup [37]. For the present setup, the relative intensity variation was modelled and validated against experimental results of sootless combustion. A typical full angle beam divergence of 50 mrad for a spray combustion case resulted in relative intensity variation of 0.5 %. As this is below the read noise of a typical high-speed camera, it is concluded that beam steering effects due to non-uniformities of the light distribution from the engineered diffuser are negligible [36].

On the collection side, the light beam is split by a long pass mirror and recorded by two high-speed cameras. Light extinction is captured using a Photron FAST-CAM SA5 high-speed camera equipped with a 50 mm Nikkor f/1.2 objective lens and a 500D close-up lens. A spectral red light filter centred at 630 nm (BW 10 nm) is mounted transmitting only light in the LED light range. Neutral density filters are fitted to adjust the light intensity such that the camera intensity resolution of 12 bit is used optimally. The camera is orientated to capture images along the spray combustion symmetric axis.

The measurements are recorded at 100 kfps with an exposure time of  $0.37 \mu\text{s}$  and a resolution of  $320 \times 192$ , which results in a pixel scale of  $0.163 \text{ mm/px}$ . With the LED light only flashing every second image, the camera alternately captures an illuminated image with extinction due to soot and a non-illuminated image with flame luminosity in the red light spectrum. The non-illuminated images are used to eliminate the flame luminosity at the time of the illuminated image. The flame luminosity

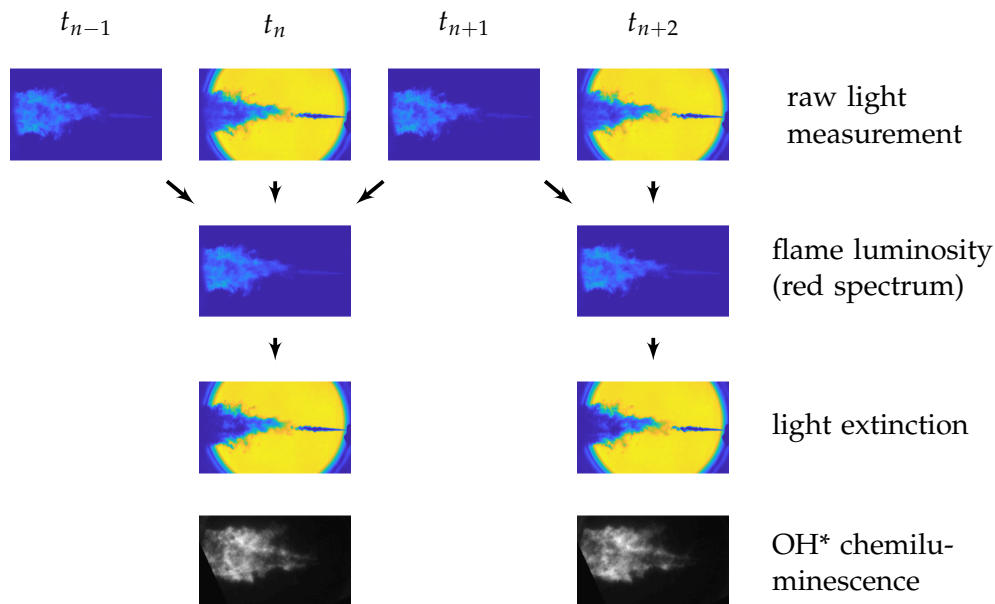


FIGURE 3.7: Camera exposure alignment and elimination of flame luminosity in the LED spectrum

is reconstructed by the arithmetic mean of the bordering two frames and subtracted thereafter from the illuminated image (see Figure 3.7). This method becomes more accurate with smaller intensity translations between each frame, i.e., by increasing the frame rate, smaller errors to the estimation can be achieved. The chosen settings are based on a previous study where different time resolutions have been tested [36].

The OH\* camera captures natural luminosity in the UV wavelength which is indicative for high-temperature combustion. The camera is equipped with a spectral filter centred at 310 nm (BW 10 nm) and a quartz glass 105 mm UV-Nikkor objective lens. As the intensity of the UV radiation is very low, it is increased using a Lambert HiCATT 18 intensifier. The incoming photons are converted into electrons, which are multiplied in a channel plate depending on the 'Gain' setting. An anode screen converts the electrons back into photons. This process is passed twice until the light signal leaves the intensifier. Light intensity can be improved by increasing the 'Gain' or prolonging exposure with the drawbacks of higher signal noise or more motion blur, respectively. An exposure time of 10  $\mu$ s and a 'Gain' setting of 770 was found to be best for the investigated fuels. All measurements are captured at a frame rate of 50 kfps with a resolution of 256x256 (pixel scale of 0.212 mm/px) and synchronized with the light extinction measurement.

### 3.3.5 Non-Ideal Camera Characteristics

In order to determine soot concentrations with extinction imaging, light intensity is used as quantitative data. With that in mind, non-ideal camera characteristics have to be taken into account to avoid misleading results.

#### Image Lag

If exposed to light, a pixel of camera sensor outputs a voltage, which is digitalised and stored in the camera memory. Exposed to no light intensity, the sensor still outputs a non-zero signal referred to as the background static level (BGs). Additionally, there is a random read noise due to camera electronics overlaying all signals. Normally, the error due to the non-zero background static level can be eliminated by subtracting it from the measured intensity. However, the background level is not constant but shows a lag when frame-to-frame intensity changes largely. This behaviour has already been observed with other cameras using a complementary metal-oxide semiconductor sensor (CMOS) and is described as a local effect for every single pixel and a global cross-pixel effect [38].

Figure 3.8 shows the characteristics for the present camera, where the top left image shows the static dark image and the top middle one the static bright image. Being exposed to an alternating light source, the dark frame after an illuminated frame indicates values lower than the static dark level. This difference is illustrated in the bottom left image and further referred to as the negative image lag  $I_L^-$ . A similar effect is observed for a bright frame after a dark frame which outputs values higher than the static bright level. It is called the positive image lag  $I_L^+$  and illustrated in the middle at the bottom.

The images show a strong local effect in the range of  $\sim 50$  intensity counts where the pattern of light intensity change can be seen in the image lag. The global effect is found to be comparatively small with  $\sim 10$  counts. Further, the image lag  $I_L$  is

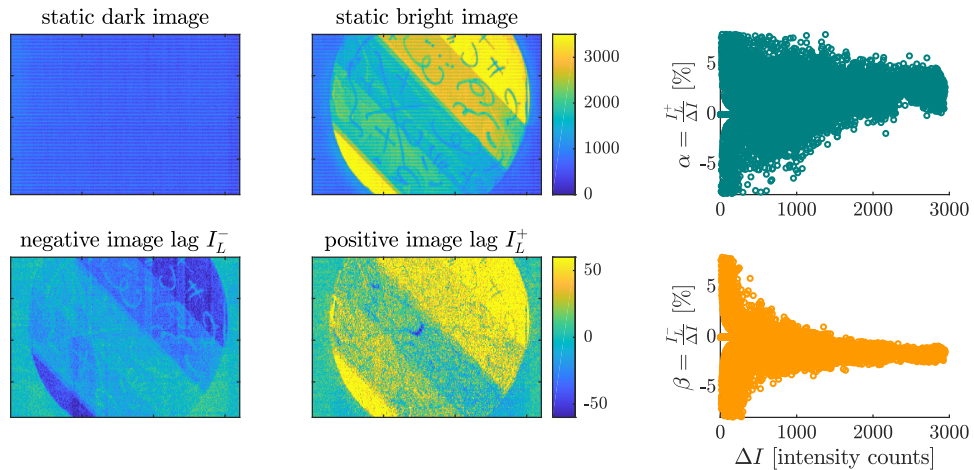


FIGURE 3.8: Image lag analysis: static dark image in the top left; static bright image in the top middle; negative image lag after bright image at the bottom left; positive image lag after dark image at the bottom middle; ratio between image lag  $I_L$  and change of intensity  $\Delta I$  on the right side

assumed to be proportional to the change in light intensity  $\Delta I$ . On the right side of Figure 3.8, the ratio between the positive image lag  $I_L^+$  and  $\Delta I$ , defined as  $\alpha$ , and the ratio of the negative image lag  $I_L^-$  and  $\Delta I$ , defined as  $\beta$ , is plotted over  $\Delta I$ . The ratio shows a constant behaviour across different changes of intensity with the positive and negative image lag being  $\sim 1.5$  percent of the local  $\Delta I$ . Interestingly, the positive image lag shows a bigger spread than the negative image lag. The increased spread for lower  $\Delta I$  is interpreted as a cause of the read noise having a larger impact when absolute intensity changes are little.

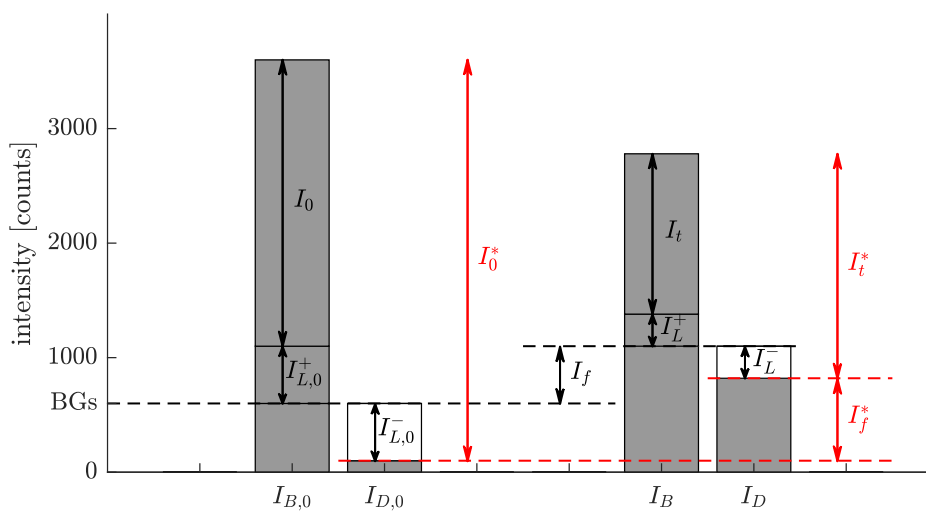


FIGURE 3.9: Schematic light extinction measurement with an alternating light source

Regarding the light extinction measurements, above-concluded behaviour can be used to eliminate the impact of local image lag. Before each combustion cycle, a non-combustion cycle is captured to define the  $I_0$  level. But as the light intensity is



alternating, the difference between the dark frame  $I_{D,0}$  and the bright frame  $I_{B,0}$  is bigger than the nominal  $I_0$  (see Figure 3.9). Regarding a combustion cycle, the static level is elevated by the flame intensity  $I_f$  and the transmitted light intensity  $I_t$  is lower than  $I_0$  due to light extinction. Again, the difference between the bright  $I_B$  and the dark frame  $I_D$  is bigger than real transmitted light intensity  $I_t$ . But, as the image lag shows a linear dependence to the change of light intensity, this error equals out when the ratio between  $I_t$  and  $I_0$  is regarded to calculate  $KL$  (see Equation 3.5). Therefore, the dark images of the non-combustion cycle are used as the reference intensity to determine  $I_0^*$ ,  $I_f^*$  and  $I_t^*$ .

$$\frac{I_t}{I_0} = \frac{I_t^* - I_L^+ - I_L^-}{I_0^* - I_{L,0}^+ - I_{L,0}^-} = \frac{(1 - \alpha - \beta) I_t^*}{(1 - \alpha - \beta) I_0^*} = \frac{I_t^*}{I_0^*} = e^{-KL} \quad (3.5)$$

### KL saturation

After eliminating the local image lag effect, only a random noise level is left, which is overlaying all intensity signals and can not be distinguished from the real intensity. In high-sooting conditions, where the transmitted intensity  $I_t$  is close to zero, this noise can cause negative values for the measured transmitted intensity. This effect is illustrated by the shaded area in Figure 3.10 on the left side and can occur for a nominal  $KL$  value greater than 3.1 with the present setup. If the measured transmitted intensity is negative, a  $KL$  value, i.e., a soot concentration can not be determined and the pixels are assigned not-a-number (NaN). This event is shown by the exemplary image on the right side, where there are dark spots in the middle of the combustion plume. It is referred to as  $KL$  saturation because the light extinction is so high that it cannot be converted into a  $KL$  value, i.e., the error of the conversion into a  $KL$  value is very large.

For soot mass calculation  $KL$  values are integrated over a predetermined area or in each pixel column. Latter is shown in Figure 3.10 at the bottom right for the exemplary image above. Hereby, the blue line represents the cross-sectional integrated  $KL$  values and the black line the number of  $KL$  saturation pixels in each pixel column. Regarding the light extinction in the combustion plume,  $KL$  saturation causes an underestimation of the present soot. This is why a second plot with the number of  $KL_{sat}$  pixels is added to the light extinction results to identify the area of erroneous data.

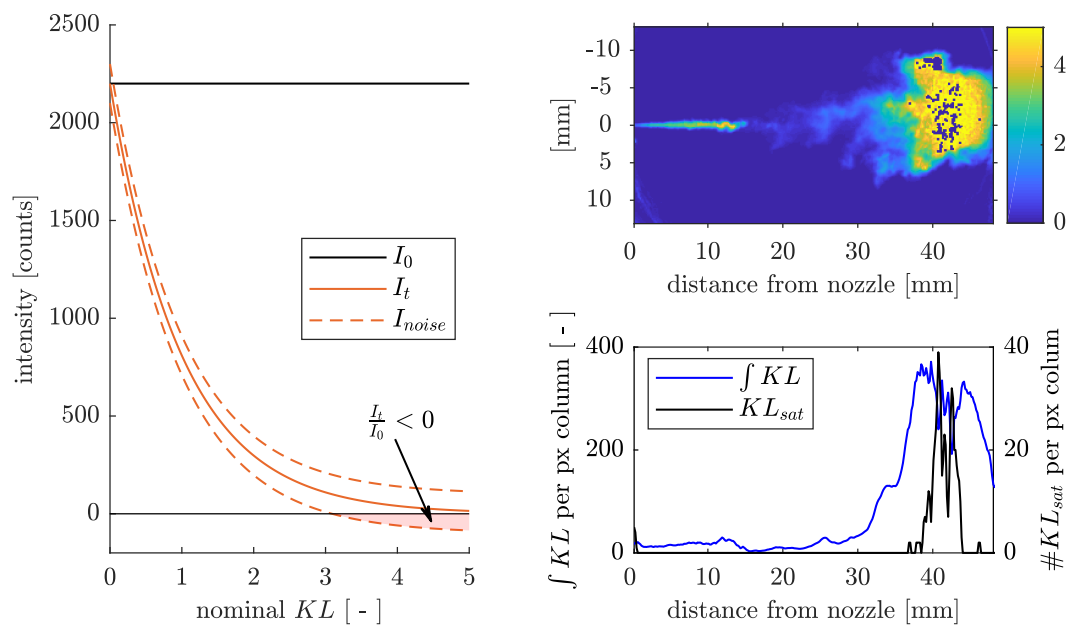


FIGURE 3.10: left: transmitted intensity plotted over nominal  $KL$  with the shaded area representing negative measured  $I_t$ ; right top: exemplary image with  $KL$  saturation; right bottom: cross-sectional integrated  $KL$  and number of  $KL_{sat}$  pixels per column

## Chapter 4

# Instrumented Engine Results

This chapter presents the results of the investigation on the Instrumented Engine test rig. First, operating parameters and the examined test conditions are introduced. Second, the combustion behaviour is analysed based on the heat release rate and brake thermal efficiency. At last, the particulate matter and gaseous emissions are presented for the glycerol emulsion and the reference diesel.

### 4.1 Instrumented Engine Test Conditions

The Instrumented Engine was fuelled with the pure reference diesel DRef and the glycerol diesel emulsion G15. Experiments were conducted over a map of selected load and turbocharge settings, while other operating parameters were kept constant as shown in Table 4.1.

The engine speed was set to 1800 rpm and the injection pressure to 650 bar. In contrast to the previous studies by Eaton et al. [6, 28] and Sidhu et al. [7], the injection timing was adjusted for every measurement such that the crank angle of 50 % cumulative heat release ( $CA_{50}$ ) was kept at a constant level. Thereby, the comparability between the fuels is increased because combustion parameters, e.g., brake thermal efficiency, are sensitive to combustion timing. The setpoint for  $CA_{50}$  is based on a sweep prior to data collection to ensure that all emissions were within the detectable range. Retarding the combustion from this setpoint had led to carbon monoxide emissions exceeding the measurement range. It is understood that this combustion timing is not efficiency optimal.

TABLE 4.1: Instrumented Engine operating parameters

Parameter	Type	Specification	
engine speed	const.	1800 rpm	
injection pressure	const.	650 bar	
injection type	const.	single injection	
$CA_{50}$	const.	1.0 CAD after TDC	
fuel	varied	DRef	G15
turbocharge	varied	no turbocharge	full turbocharge
engine torque	varied	20 Nm   50 Nm   80 Nm   110 Nm   140 Nm	

Both fuels were assessed at engine torques from 20 Nm to 140 Nm, once without turbocharge and once with full turbocharge (see Table 4.1). The latter is expected to overcome the poor ignition properties of glycerol.

## 4.2 Combustion Behaviour

To examine the combustion behavior, the in-cylinder pressure is considered. The data were recorded after a stabilisation phase of 30 s over a minimum of 30 combustion cycles and averaged thereafter. The results are illustrated in Figure 4.2, which shows the apparent heat release rate as a solid line and the in-cylinder pressure as a dashed line plotted over crank angle degree. The heat release rate is calculated based on the engine's geometric specifications and a constant ratio of the specific heats of  $\gamma = 1.28$  [9]. It is noticed that the AHRR shows a slight offset from zero before combustion, which might be caused by heat transfer which is neglected in the AHRR calculation. The vertical black line in Figure 4.2 indicates  $CA_{50}$ , where 50 % of the combustion energy is released. The dash-dotted lines represent the injection period for each fuel, which was adjusted to achieve above mentioned combustion timing. The illustrated period is based on the ECU signal, which is apparently longer than the needle lift duration since it is disproportional to fuel consumption. Comparing the injection duration between the fuels, a longer period for the G15 is observed, which can be explained by its lower heating value.

Without turbocharge, the chemical energy is released in a single peak, while with full turbocharge and increasing load, the AHRR shows a second peak and a lower maximal heat release rate. It is noticed that at high engine loads the initial heat release advances beyond a usual efficiency orientated combustion timing. However, this does not affect the comparability between the fuels. Regarding the differences, the G15 results in a retarded but faster heat release. This behaviour is present with the G15 being injected earlier, similar, and later than the DRef (see no turbocharge 80 Nm, full turbocharge 110 Nm, and no turbocharge 140 Nm, respectively).

To differentiate between effects, Figure 4.1 shows the difference between SOI and  $CA_{10}$ , indicative for the ignition delay, and the difference between SOI and  $CA_{50}$ . The ignition delay is decreasing for both fuels with increasing engine load, which

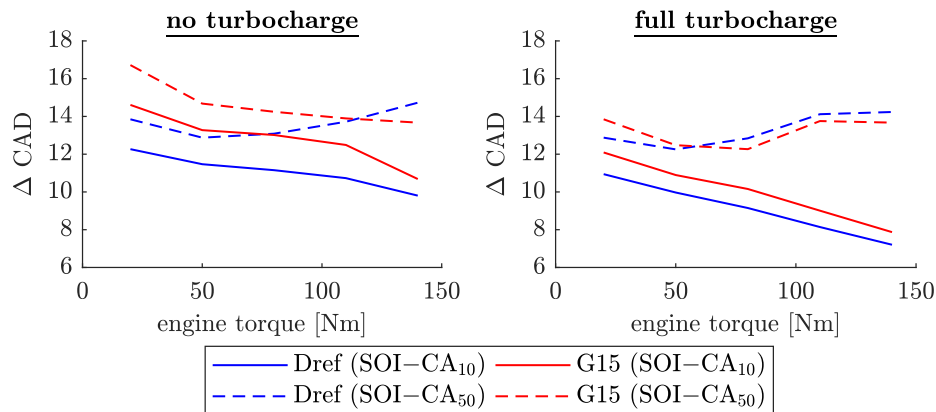


FIGURE 4.1: Ignition delay and combustion delay

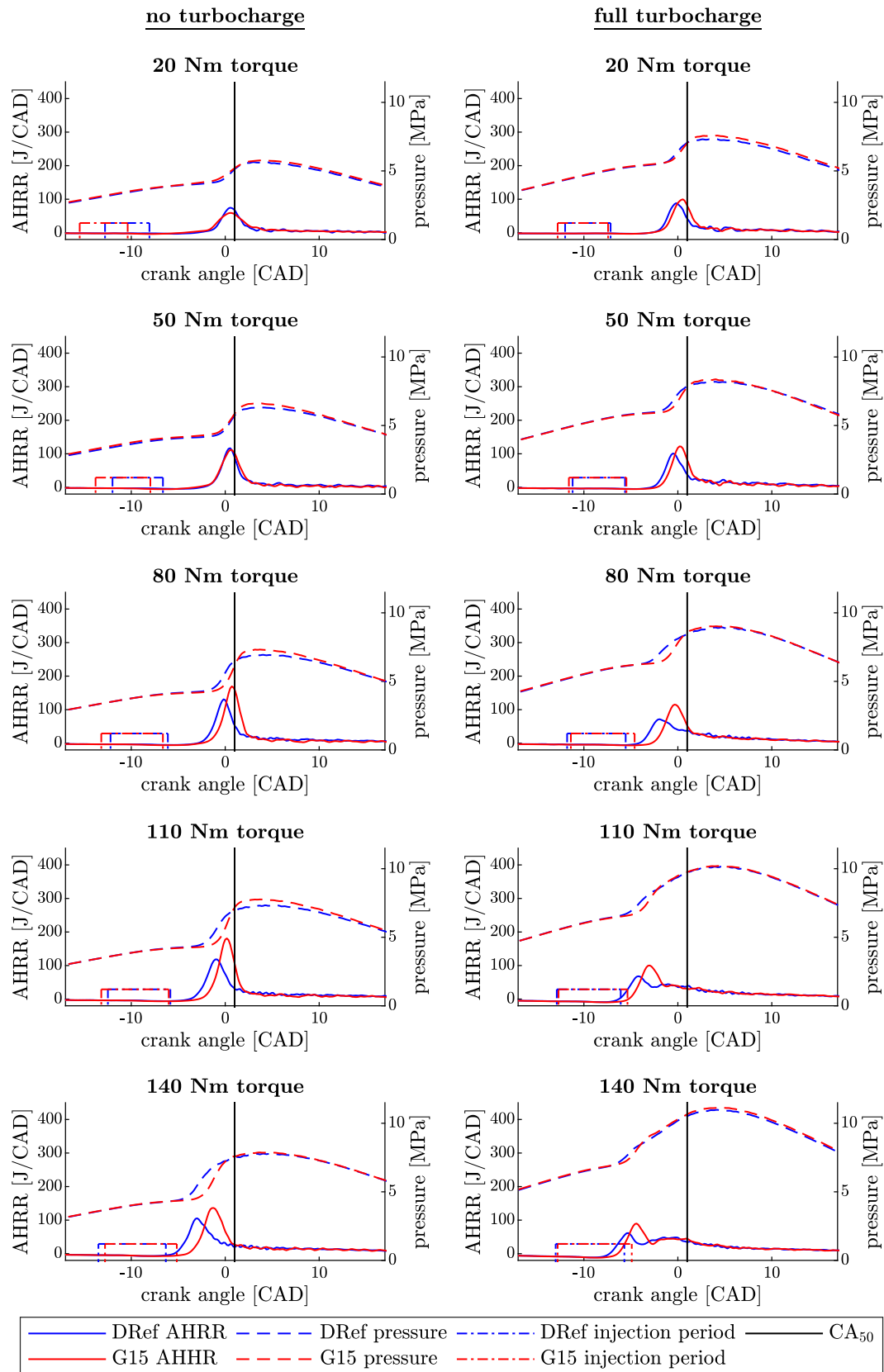


FIGURE 4.2: Ensemble of AHRR plots of the Instrumented Engine: solid line: AHRR; dashed line: in-cylinder pressure; dash-dotted line: injection period; vertical black line: CA<sub>10</sub>

is likely to be caused by engine heating. Comparing the fuels, the G15 constantly features an increased delay, which is affected little by engine load. Regarding the difference from SOI to CA<sub>50</sub>, the G15 has a longer combustion delay at low loads, but a shorter delay at high loads, despite the longer ignition delay.

In conclusion, the glycerol emulsion resulted in an increased ignition delay and a faster heat release. Whether the more intense combustion is caused by the oxygen content of the fuel or by more premixed air fuel mixture being available due to the prolonged ignition, could not be distinguished.

Additionally to the pressure derived analysis, the brake thermal efficiency (BTE) was examined. BTE was calculated according to Equation 4.1 with the power input being specified by the fuel consumption and the lower heating value LHV. The power output is determined by the engine speed and the generated torque. As shown in Figure 4.3, there are no significant changes in BTE noticeable with absolute deviations being less than 0.8 % across all conditions. Improved brake thermal efficiency of 2 % as reported by Sidhu et al.[7] could not be confirmed. The previously detected improvement is assumed to be caused by differences in combustion timing which was not adjusted. The value for G15 at the highest load without turbocharge is not illustrated as the measured fuel consumption was unreasonably low (BTE = 210 %).

$$BTE [\%] = \frac{2\pi n T_{dymo}}{\dot{m}_{fuel} LHV_{fuel}} \quad (4.1)$$

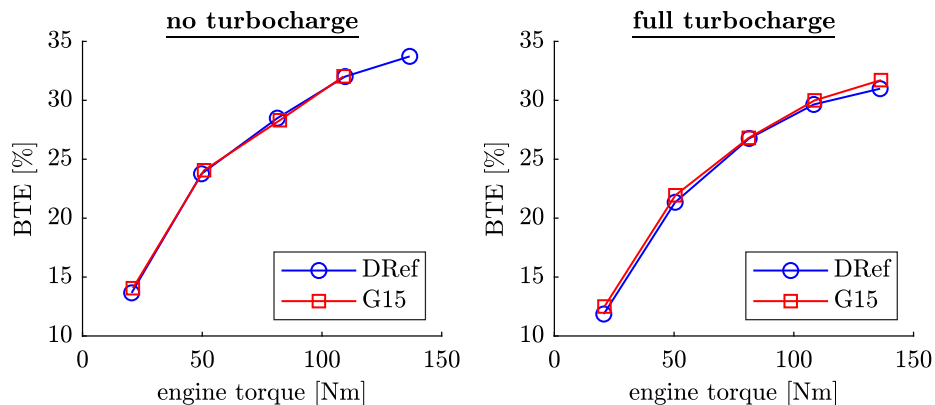


FIGURE 4.3: Brake thermal efficiency of the Instrumented Engine

## 4.3 Emissions

Pollutant concentrations were recorded over a period of 1 minute and averaged thereafter. PM and gaseous emissions were hereby sampled simultaneously.

### 4.3.1 Particulate Matter Emissions

While previous studies have indicated a reduction of PM emissions by measuring the smoke opacity [6, 7], it was investigated whether this effect can be confirmed with the current setup. In contrast to the single-value smoke opacity measurement,

emissions were examined with a fast particulate spectrometer. It provides the number size distribution, which is presented on a volumetric basis.

### Small Particles

When using the glycerol emulsion, a sharp and large peak in the diameter range of 5 to 10 nm is observed. With the DRef, no such behaviour is noticed with the number of particles in that size range being less than 1 % of the G15. The number of particles emitted by the glycerol is rising with increasing engine load, which is indicated by increasing colour intensity in Figure 4.4.

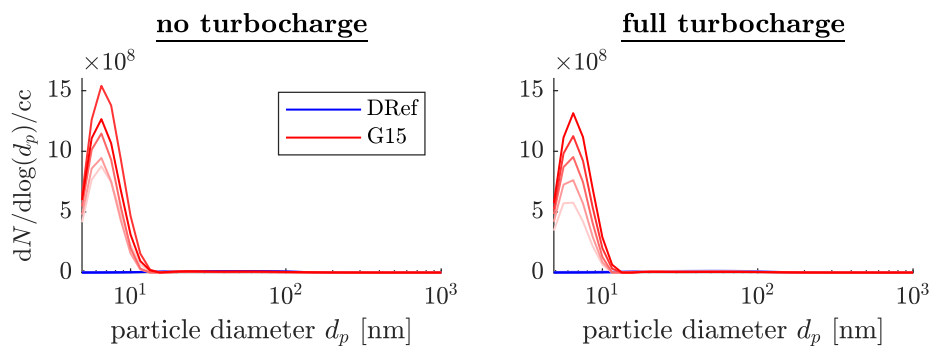


FIGURE 4.4: Particle number size distribution: increasing colour intensity represents rising engine load.

Having identified this very particular emission behaviour of the glycerol emulsion, properties and origin of these particles were further investigated. Exhaust particulate emissions were sampled on a glass fibre filter at the location of the particulate matter analyser. The collection was conducted with an engine torque of 50 Nm and full turbocharge. After collection, the sample for the DRef was black, whereas the colour of the G15 particle sample was brown. With soot being known to be black, this is an indication that the G15 particulate emissions contain a larger fraction of non-soot particles.

In the next step, both samples have been investigated using thermogravimetric analysis. It has to be mentioned, that this analysis is only conducted for a single sample per fuel due to the high expenses for collection and analysis. Therefore, the reproducibility of the results is not proven, which is why they shall only be used as a first indication.

The temporal development of the furnace temperature and the sample weight is illustrated in Figure 4.5 with the weight being normalized to its initial value. First, the samples were heated under inert atmosphere, where moisture and volatile compounds are expected to dissipate. After a cool-down phase, the same sample was exposed to oxidant atmosphere, which leads to oxidation of soot particles [39]. The largest weight fraction of the sample were glass fibres, which were found to have a weight loss of less than 2 % during the thermogravimetric analysis.

Regarding the devolatilisation of the DRef and the G15 sample, both lose mass similarly until the temperature reaches 100 °C. This is probably caused by moisture evaporation. Afterwards, the G15 sample weight decreases more than the DRef leading to difference in mass loss during the stationary phase at 550 °C. With further

increasing gas temperature, both samples lose more weight, with the effect being more significant for the DRef. With oxidant atmosphere, both samples reduce their weight further, where the total mass loss of DRef is greater than of G15.

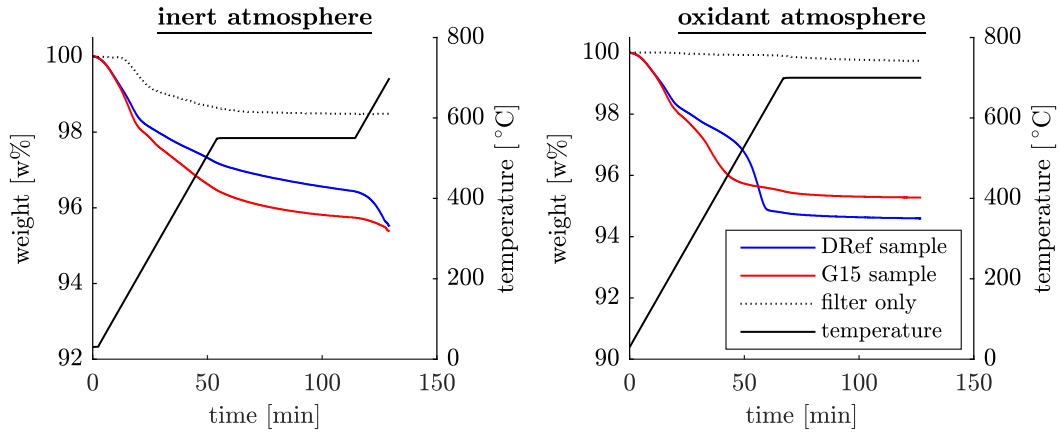


FIGURE 4.5: Thermogravimetric analysis of exhaust particulate emissions sampled on a glass fibre filter

To compare the samples regarding their volatile content, the ratio between the devolatilisation weight loss from 100 °C to 550 °C and the total oxidation weight loss is calculated. As shown in Table 4.2, this ratio is higher for the G15 sample, which can be interpreted as a volatile to soot ratio. It indicates that the large peak at small diameters using the glycerol emulsion might be partly or entirely caused by condensed volatile compounds. However, the increasing number of particles with engine load shows that the issue can not be counteracted by high load operating conditions.

TABLE 4.2: particulate matter filter samples

Parameter	DRef	G15
$\frac{\Delta w_{inert, 100-550^{\circ}\text{C}}}{\Delta w_{oxidation}}$	$\frac{3.05\%}{5.41\%} = 0.56$	$\frac{3.73\%}{4.72\%} = 0.79$

In conclusion, the large peak of small particles is an issue that has to be considered. If the particles are small solid soot particles, they are especially harmful due to their penetration ability. Being volatile compounds, they feature enhanced combustion resistance which has to be overcome. The thermogravimetric analysis was not able to clarify the origin as expected. The particles might also be related to impurities of the glycerol. In a study on glycerol as a boiler fuel, left-overs of soluble catalysts are reported to cause high PM emissions [24]. There will be on-going investigations on the origin and properties of the small particle peak based on numerical simulations and transmission electron microscopy.

### Large Particles

By changing the ordinate scale of the PM measurements, a soot characteristic peak is observed for both fuels as illustrated in Figure 4.6. When analysing the results, it has to be considered that in the particulate matter analyser the exhaust sample is diluted in order to meet the optimum between signal strength and long cleaning



intervals. This dilution is automatically taken into account by the analyser when outputting the number size distribution. However, the applied dilution factor varied significantly between the fuels due to the large difference in the number of small particles, ranging from 90 to 240 for the DRef and 730 to 890 for the G15. Thus, the large particle emissions of the G15 may not be recorded with optimal dilution.

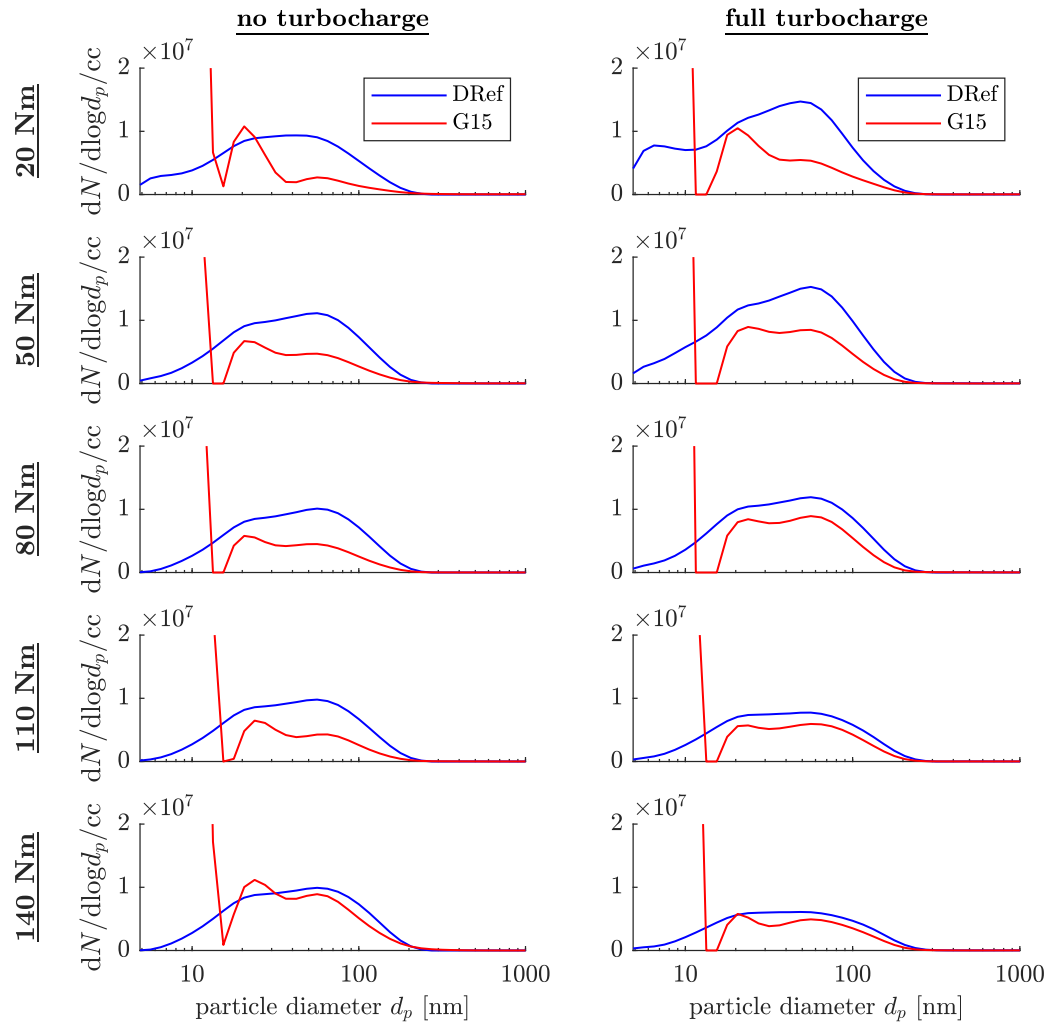


FIGURE 4.6: Detailed view of the particle number size distribution

Interestingly, the small particle peak and the large particle peak of the G15 are separated by a diameter range where no or very few particles are detected. This is interpreted as an indication that the peaks are from a different origin.

Comparing the two fuels, the glycerol emulsion emits less particulate matter with diameters greater than 25 nm, while the biggest reduction is achieved at a particle size around 60 nm. This effect is most significant at low engine loads and is reduced with increasing torque. Without turbocharge, the number of particles with diameters greater than 25 nm is reduced by 61 % at 20 Nm, by 56 % at 80 Nm, and by 11 % at 140 Nm. Turbocharge increases the convergence between the fuels.

Effective mechanisms can be derived from the correlation with engine load and turbocharge. While load increases combustion and exhaust temperatures, turbocharge raises ambient gas temperatures in the cylinder. Both enhance ambient reactivity

and soot oxidation, which is why the impact of fuel reactivity and volatility is reduced. Thus, it would be expected that at high loads, the inherent oxygen of the low reactive glycerol is released easier and PM reductions are more significant. However, inverse behaviour is observed. It is therefore concluded, that the PM reduction is only partly achieved due to the fuel oxygen content, while physical-driven effects contribute largely at low engine loads.

### 4.3.2 Gaseous Emissions

Gaseous emissions were examined for carbon monoxide CO, total unburned hydrocarbons THC, and nitrogen oxides NO<sub>x</sub>. The latter is calculated as the sum of the separately determined NO and NO<sub>2</sub> emissions. Pollutant concentrations were measured as volume fractions ( $f_v$ ) and converted to a brake specific basis according to Equation 4.2. Hereby,  $P_{out}$  is the generated power, and  $\dot{m}_{exhaust}$  is the exhaust mass flow.  $MW_{exhaust}$  is the molecular weight of the exhaust gas, which is set to 29.40, and  $MW_i$  is the molecular weight of the pollutant  $i$  with  $MW_{CO} = 28.01$ ,  $MW_C = 12.01$ ,  $MW_{NO} = 30.01$ , and  $MW_{NO_2} = 46.01$  [9].

$$BSE_i = \frac{f_{v,i} \dot{m}_{exhaust} MW_i}{P_{out} MW_{exhaust}} \quad (4.2)$$

Figure 4.7 illustrates the cylinder-out carbon monoxide emissions on the left and the THC emissions on the right. Both pollutants indicate incomplete combustion and follow similar trends. The highest brake specific emissions are measured at the lowest load without turbocharge, while increasing load and turbocharge reduces both, CO and THC.

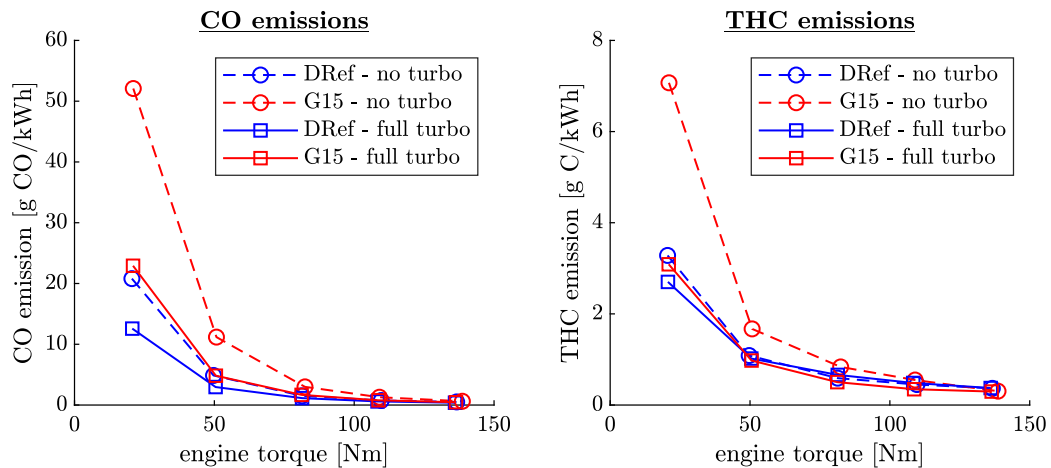


FIGURE 4.7: Carbon monoxide and total unburned hydrocarbon brake specific emissions

Comparing the G15 to the DRef, the glycerol emulsion increases both pollutants, which matches the behaviour that is observed in previous studies [6, 7]. With twice as high CO emissions at low loads, this effect is significant. The ratio between CO emitted with G15 and CO emitted with DRef is decreasing with increasing load. The increase in incomplete combustion products can be explained by to the low reactivity of glycerol.

Regarding nitrogen oxide emissions, differences between the fuels are less significant. A slight reduction is observed for the G15 at high loads and full turbocharge. A correlation between PM and NO<sub>x</sub> emissions is not noticed.

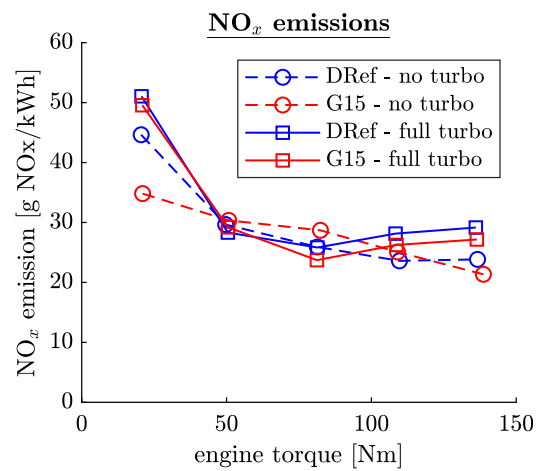


FIGURE 4.8: Nitrogen oxide emissions

In summary, it can be shown that the glycerol emulsion increases incomplete combustion pollutants significantly, but has little impact on nitrogen oxides.



## Chapter 5

# Optical Engine Results

This chapter presents the results of the optical investigation of the glycerol emulsion. First, the operating parameters and test conditions are introduced. Second, the results of the OH\* Chemiluminescence are presented, followed by the light extinction measurements. In contrast to the Instrumented Engine, the glycerol emulsion was not only compared to the pure reference diesel, but also to a 25 w% TPGME diesel mixture, representing a benchmark fuel blend.

### 5.1 Optical Engine Test Conditions

The Optical Engine was operating at 500 rpm with fuel being injected at 1000 bar. The start of injection was chosen to 4 CAD before TDC, which resulted in ignition occurring around TDC for the lowest temperature condition and about 2 CAD before TDC for the highest temperature condition. The injection duration was set to 4 ms, which equals 12 CAD, to ensure that a steady combustion phase was captured. For each fuel and condition, 30 injections were recorded, which were split into three runs of 10 injections each. To avoid residuals of a previous combustion cycle affecting the measurements, the engine was operating in a skip-fire mode, having 10 non-combustion cycles between each injection.

TABLE 5.1: Optical Engine operating parameters

Parameter	Specification
engine speed	500 rpm
injection pressure	1000 bar $\pm$ 10 bar
start of injection	4 CAD before TDC
injection duration	4 ms = 12 CAD
number of injections	3 $\times$ 10
number of skip-fire cycles	10

All fuels were assessed under the three conditions listed in Table 5.2. The conditions represent different ambient gas temperatures with Condition 1 being the lowest temperature case and Condition 3 the highest temperature case. Gas properties at TDC were estimated based on the zero-dimensional engine model and the tuned compression ratio described in Section 3.3.2. Inlet pressure was chosen such that the gas density at TDC is kept constant.

TABLE 5.2: Optical Engine Condition Points

Parameter	Cond. 1		Cond. 2		Cond. 3	
inlet pressure	1.262	bar	1.406	bar	1.550	bar
inlet temperature	55.0	°C	92.5	°C	135.0	°C
pressure at TDC	38.62	bar	41.67	bar	44.63	bar
density at TDC	16.65	kg/m <sup>3</sup>	16.65	kg/m <sup>3</sup>	16.65	kg/m <sup>3</sup>
temperature at TDC	808.0	K	871.9	K	933.7	K

### Comparison of Injected Fuel Mass

Using the optical measurements, the soot mass concentrations in the combustion plume are determined. However, the injected fuel mass and the injected energy are not constant when varying the fuel. To ensure that differences in soot behaviour are not caused by different amounts of injected energy, the fuel mass injected into a sealed beaker after 1000 injections was compared using the same injector, fuel pressure and fuel pump (see Table 5.3).

TABLE 5.3: Comparison of Injected Fuel Mass and Injected Energy

Fuel	$N_{inj}$	$N_{rep}$	$\bar{m}_{inj}$	$\Delta\bar{m}_{inj}$	$\Delta\bar{m}_{inj}LHV$
DRef	1000	3	10.68 g	0.0 %	0.0 %
G15	1000	3	11.41 g	6.8 %	-2.9 %
T25	1000	3	10.99 g	2.9 %	-6.3 %

The injected mass of the G15 and the T25 is higher compared to the reference diesel following the same order of the fuel density. Taking the heating value of the fuels into account, the injected energy of G15 and T25 is lower than of the DRef. However, the variation among the fuels is comparatively low, which is why its impact on soot behaviour is neglected.

## 5.2 OH\* Chemiluminescence

To start the optical analysis, the OH\* chemiluminescence measurements are regarded. They are used to determine the ignition delay, the flame lift-off length, and the quasi-steady period.

### 5.2.1 Ignition Delay Time

The examination of a stochastic parameter like the ignition delay and other upcoming parameters is based on the average over several injections. In order to assess the reliability of the averaged value, the 95 % confidence interval is calculated, which is expected to bracket the true mean 95 % of a time [40]. Additionally to the variance of a measurement, it takes into account that the averaged value and the true mean converge with increasing number of measurements.

$$CI_{95\%} = \bar{X} \pm t_{95\%} \frac{s}{\sqrt{n_m}} \quad (5.1)$$

The confidence interval is calculated according to Equation 5.1, where  $\bar{X}$  is the arithmetic average of the measurements,  $s$  the standard deviation,  $n_m$  the number of measurements, and  $t_{95\%}$  the percentile of the  $t$  distribution. In this study the number of measurements equals  $n_m = 30$  injections, resulting in  $t_{95\%}(n_m = 30) = 2.045$  [40].

The ignition delay time (IDT) is determined from the time difference between start of injection and the first OH\* intensity. The latter showed a step increase compared to its background noise, thus ignition was clear to identify. Start of injection is determined based on the light extinction images to rule out any errors due to a trigger delay in the injection system.

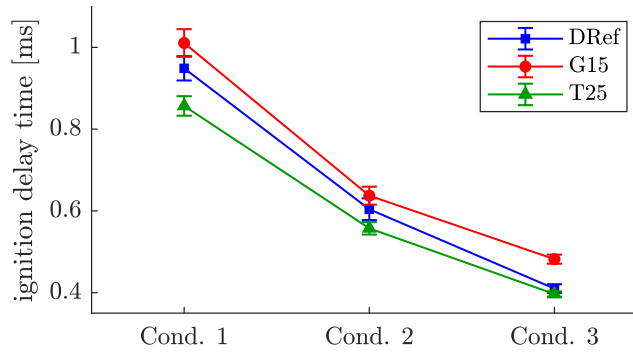


FIGURE 5.1: Ignition delay time based on the first OH\* intensity with the bar showing the 95 % confidence interval

Figure 5.1 shows the mean ignition delay time for all fuels with the bar representing the 95 % confidence interval. The ignition of the G15 is retarded compared to the reference diesel. Interestingly, this effect is present across all conditions and does not decrease with rising ambient temperature. The T25 has a shorter ignition delay at low temperatures, which is consistent with the higher cetane number of the TPGME. With increasing temperatures, the delay times of T25 and DRef converge.

The measurements for all 30 injections are illustrated in Appendix B.2. It also shows the confidence interval of each 10 consecutive recorded injections compared to the confidence interval of all 30 injections. At the lowest temperature condition, an offset between the consecutive recorded injections is observed, which reduces the reliability of the IDT measurements at Condition 1. The offset might be caused by an increased head bulk temperature due to previous runs. Within the consecutive recorded injections, a slightly decreasing trend is observed, which is considered to be caused by increasing wall temperatures. With exception to the lowest temperature condition, the confidence intervals overlap and thereby indicate reproducibility.

### 5.2.2 Flame Lift-off Length

While the ignition delay indicates the fuel air mixing time prior to combustion in the premixed combustion phase, the flame lift-off length is an indicator for fuel air mixing during the quasi-steady combustion phase. To analyse the behaviour during this combustion period, the instantaneous flame lift-off length is regarded. It is determined by the integrated OH\* intensity in each pixel column, which is representative for a specific distance to the injector nozzle. This cross-sectional integrated

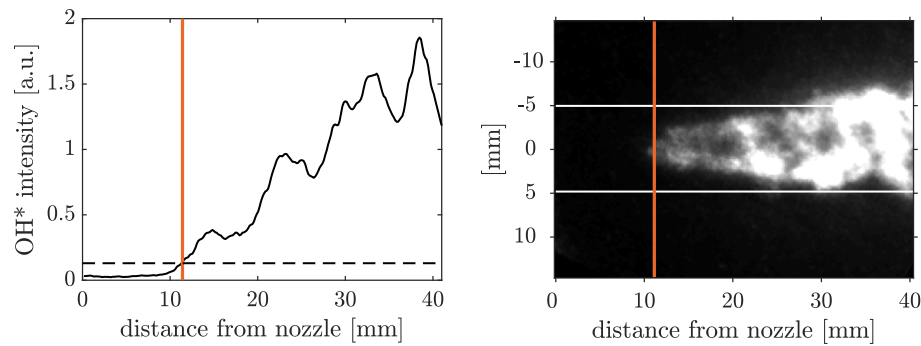


FIGURE 5.2: Exemplary determination of the instantaneous FLOL (red line) by the cross-sectional integrated OH\* intensity (solid black line) passing a threshold value (dashed line) (exemplary OH\* image on the right side: DRef Cond. 3 Inj. 3 Frame 150)

intensity is calculated in an area close to the centreline as represented by two white lines in Figure 5.2 on the right side. The instantaneous flame lift-off length is then determined by this value passing an arbitrary threshold of 0.13 (see Figure 5.2 on the left). As the slope of cross-sectional integrated OH\* intensity is similar among the fuels, the threshold value has little impact on the differences between the fuels.

Figure 5.3 shows the temporal FLOL development averaged over all injections with the coloured shade indicating the 95 % confidence interval. After a wide spread at ignition, the FLOL stabilises at a constant level before the end of the injection period leads to a break-up. While fuels ignite downstream of the stable level at Condition 1, they ignite slightly upstream at Condition 3. Increasing ambient temperature results in a decrease of the FLOL for all fuels with differences between the fuels narrowing. Compared to the DRef, the G15 and the T25 feature a 2.5 mm and 2.0 mm increased FLOL at the low temperature condition, whereas at the high temperature condition all fuels show a very similar behaviour. Based on this data the quasi-steady period is identified to begin at 2.5 ms and end at 3.8 ms after start of injection.

Figure 5.4 illustrates the averaged OH\* intensity over the quasi-steady period which is constructed from a total of 1950 frames for each fuel and condition. The vertical

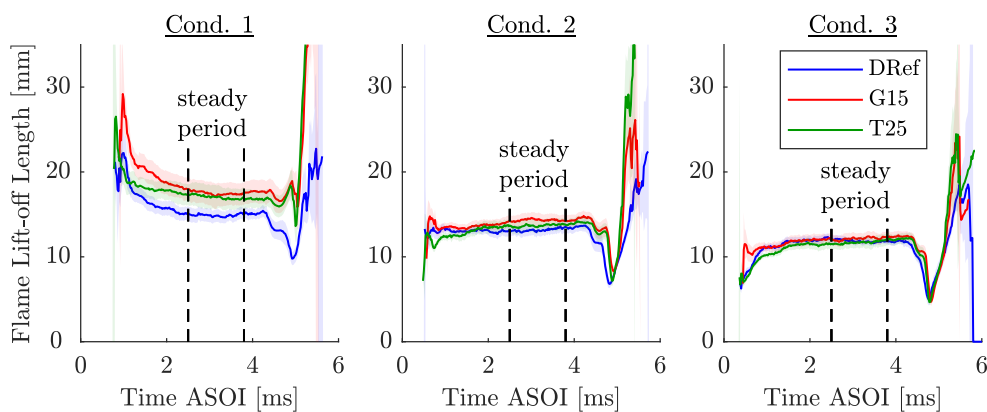


FIGURE 5.3: Flame lift-off length over time after start of injection with the shaded area representing the 95 % confidence interval



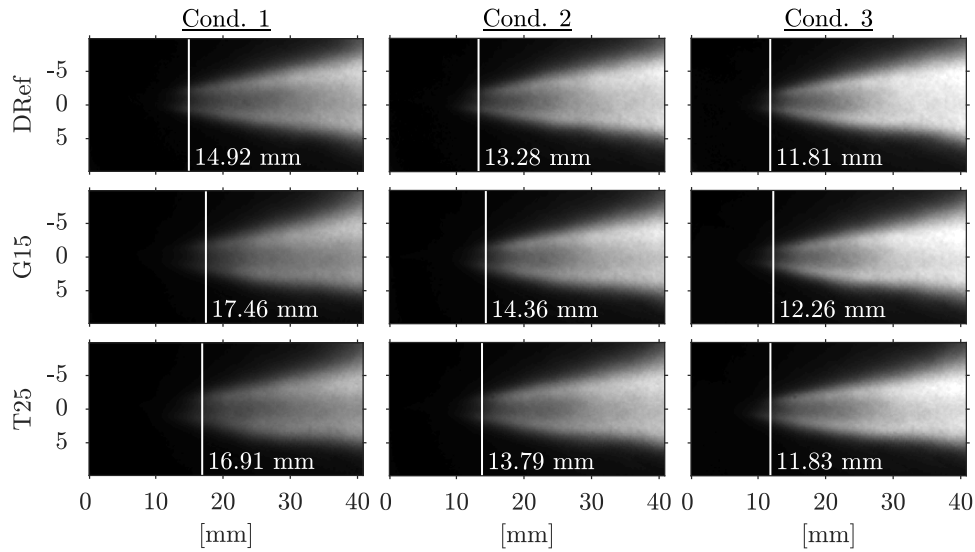


FIGURE 5.4: Averaged OH\* intensity over quasi-steady period with the flame lift-off length indicated by the white line

white line represents the FLOL with the value being shown aside, which is calculated from the average of the instantaneous flame lift-off length during the quasi-steady period.

The FLOL of all 30 injections is illustrated in Appendix B.3. The confidence intervals of each 10 consecutive recorded injections overlap largely with the confidence interval of all 30 injections for all fuels and conditions. Trends within the consecutive recorded injections are not observed.

## 5.3 Light Extinction Measurements

Having identified the quasi-steady period based on the OH\* measurements, the light extinction measurements are divided into a premixed combustion phase and a quasi-steady phase. This is done because the combustion plume was travelling outside the observable area, thus the peak soot concentration may not be recorded. Therefore, an evaluation of the total soot mass formed was not possible, which is why the soot behaviour is assessed firstly as a spatial gradient during the quasi-steady combustion phase, and secondly as a temporal gradient in the premixed phase before the plume exits the observable area. A similar technique has already been used by Bjørgen et al. [29] and yielded reasonable results.

All images are processed as  $KL$  values which can be proportionally converted into a soot mass in case the light extinction is due to soot particles according to Section 3.3.3.

### 5.3.1 Spatial Soot Gradient in Quasi-Steady Period

Assuming that the speed of the combustion plume is similar for all fuels, the spatial soot gradient is an indicative parameter of the soot behaviour. To determine the

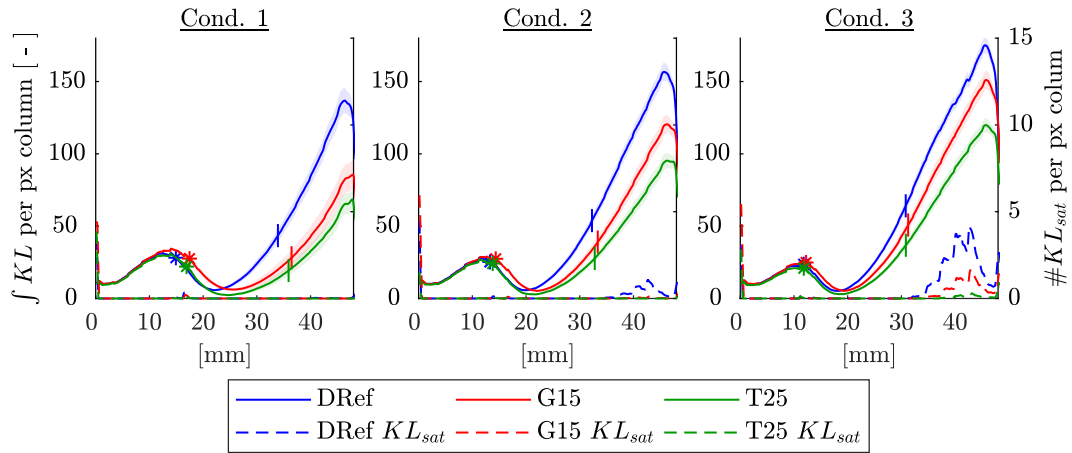


FIGURE 5.5: Integrated  $KL$  per pixel column (solid line) and number of  $KL_{sat}$  per pixel column (dashed line) during the quasi-steady phase with the star representing the FLOL and the vertical line showing 19 mm after FLOL

spatial soot gradient the  $KL$  values are integrated in each pixel column and plotted over the distance from the injector nozzle. Figure 5.5 illustrates the average over all 30 injections of this cross-sectional integrated value as a solid line with the shaded area representing the 95 % confidence interval.

Describing the plot from the injector nozzle onwards, the first peak shows the light extinction caused by the liquid fuel core, which is increasing in the beginning because of the divergence of the spray and decreasing further downstream due to fuel evaporation. The rise after the minimum indicates the rising soot concentration with increasing distance from the injector nozzle. These results are reliable until  $KL$  saturation occurs, which is indicated by the dashed line that illustrates the number of  $KL$  saturated pixels per column. It shows that the results of the DRef and the G15 at the highest condition are not reliable after 32 mm distance to the injector nozzle. The drop of the cross-sectional integrated  $KL$  at the end is caused by the circular chamber wall reducing the observable area.

Comparing the three fuels, the G15 shows an increased liquid penetration length with the effect being most significant at Condition 1, while the T25 and DRef have similar liquid lengths. Further impacts on the spray due to the two-phase fuel are not observed. Possible effects could be the separation of diesel and glycerol droplets due to their difference in volatility or differences in the spray cone angle due to non-uniform fuel viscosity. The similarity of the spray characteristics is shown in Figure 5.6. With rising temperatures, soot is observed closer to the injector and the spatial gradient increases for all fuels. Within each condition the DRef has the biggest increase and the T25 the lowest. The G15 is closer to the T25 at the low temperature condition and looks centred between the DRef and the T25 at the high temperature condition.

For further comparison to other parameters, a single value is extracted. The spatial soot gradient SSG is the maximal increase of soot mass between the FLOL and 19 mm after the FLOL. Hereby, erroneous data due to  $KL$  saturation are avoided. By relating the spatial gradient to the FLOL instead of the injector nozzle, the variation

of the flame location is taken into account. In Figure 5.5, the FLOL is marked with a star and the location of 19 mm after the FLOL is indicated by the vertical line. The increase of soot mass is calculated from the mass difference over  $\Delta x = 1.63$  mm distance, in order to smooth out large pixel to pixel fluctuation (see Equation 5.2).

$$SSG = \max \left( \frac{m_{soot}(x) - m_{soot}(x - \Delta x)}{\Delta x} \right) \quad x \in [FLOL, FLOL + 19 \text{ mm}] \quad (5.2)$$

The SSG of all 30 injections is illustrated in Appendix B.4. No trends between or within the consecutive recorded injections are noticed.

Figure 5.6 shows the averaged KL image over the quasi-steady period with the SSG being displayed at the bottom. Pixels with KL saturation are omitted in the construction of the averaged image.

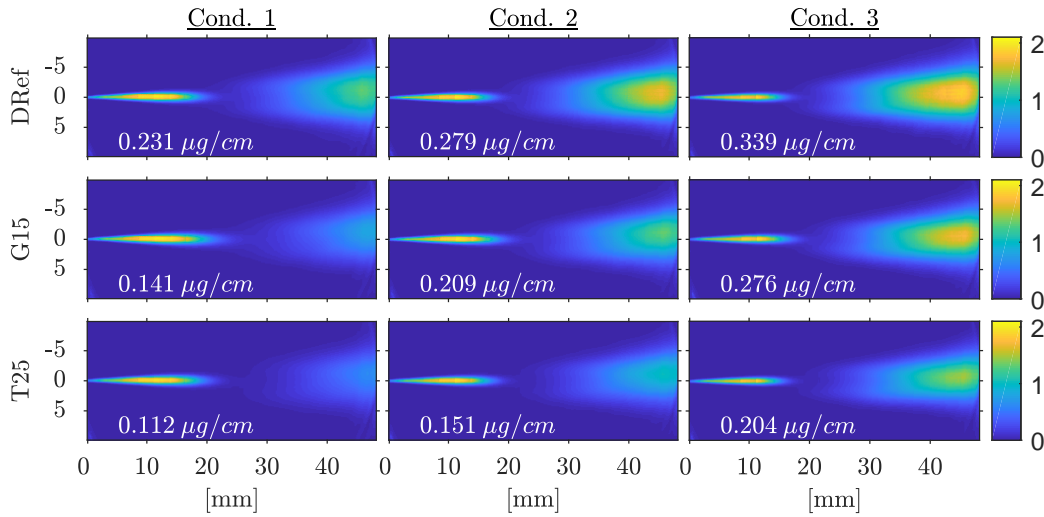


FIGURE 5.6: Averaged KL plots during the quasi-steady period with the bottom value indicating the soot gradient between the white lines

### 5.3.2 Temporal Soot Gradient in Premixed Combustion Phase

In addition to the soot behaviour during the quasi-steady period, the soot formation in the premixed combustion phase is assessed. Hereby, the total soot mass present in the combustion plume can be examined until the plume exits the observable area. Figure 5.7 illustrates the temporal development of the light extinction measurements for the highest temperature condition. Each image is averaged over all injections while KL saturation pixels are omitted. The ensemble shows the combustion plume leaving the observable area at around 1 ms after SOI.

In order to further assess the behaviour in the premixed phase, the total soot mass in the observable area is integrated and plotted over time after start of injection with the colour shaded area representing the 95 % confidence interval (see Figure 5.8). The vertical black line represents when the combustion plume reaches the end of the observable area opposite to the injector. The grey shaded area indicates  $\pm$  the standard deviation of the exit time. However, the combustion plume travelling outside

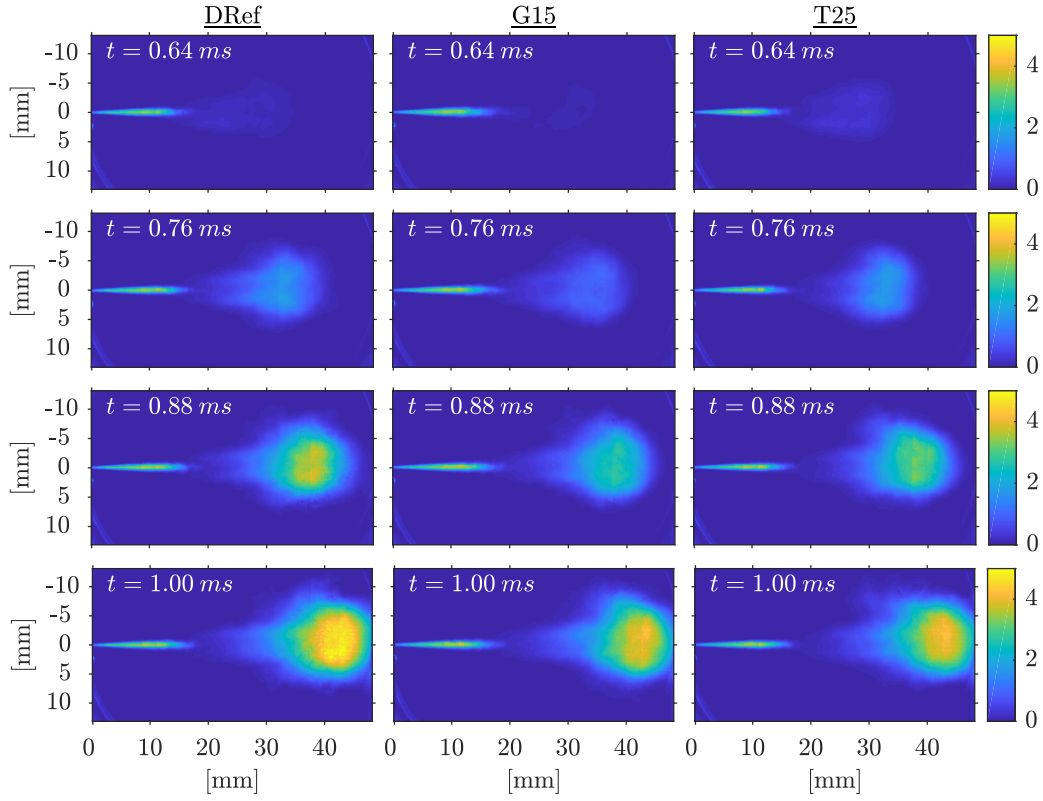


FIGURE 5.7: Temporal development of the  $KL$  during premixed phase averaged over 30 injections for the highest ambient gas temperature condition

the observable area is only limiting the temporal investigation at condition one and two. At the high temperature condition,  $KL$  saturation limits the time interval of reliable values, which is illustrated by the dashed plots representing the number of  $KL$  saturation pixels.

With rising ambient temperatures, soot formation starts earlier and increases faster. The offset from zero prior to ignition is caused by the area of integrated  $KL$  including the tip of the liquid core to ensure that all soot produced is considered. As the area of integration is kept constant among the fuels, this offset is most visible for the G15 with the longest penetration length.

For the lowest temperature condition, soot formation can only be observed after the front of the fuel air plume has already left the observable area, which is why it is not further investigated. Regarding the conditions two and three, the initial soot formation of the G15 is delayed, while DRef and T25 start to form soot at a similar time after start of injection. Afterwards, the soot mass of the DRef increases faster than of the T25, which is consistent with the soot reducing effect of TPGME. However, such an effect cannot be observed for the G15, which features in a similar temporal soot increase like the DRef.

$$TSG = \max \left( \frac{m_{soot}(t) - m_{soot}(t - \Delta t)}{\Delta t} \right) \quad t \in [IDT, IDT + 0.30 \text{ ms}] \quad (5.3)$$

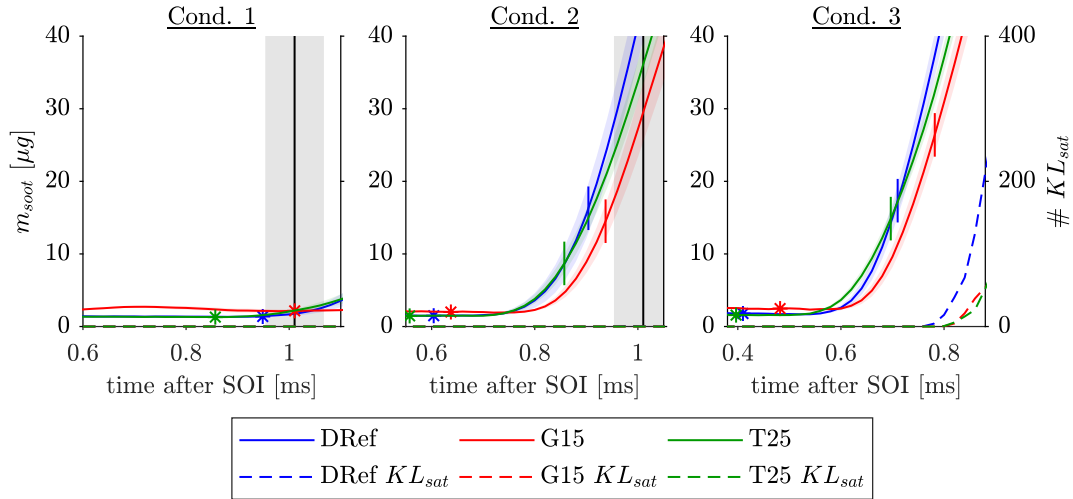


FIGURE 5.8: Temporal development of the soot in the premixed combustion phase. The vertical black line indicates when the combustion plume reaches the end of the observable area, the star represents ignition, and the small vertical line shows 0.3 ms after ignition.

To take the different combustion stage into account, ignition is marked with a star in Figure 5.8. Similar to the spatial soot gradient, a temporal soot gradient TSG is extracted as the maximal temporal soot increase within 0.30 ms after ignition. Hereby, data points with  $KL_{sat}$  are not included which is shown by the dashed plots showing zero before the end of the considered time interval, illustrated by the small vertical lines. The gradient is determined according to Equation 5.3 with a time step of  $\Delta t = 0.02$  ms. The extracted values are shown in Table 5.4, while the TSG of all injections at Condition 2 and Condition 3 is illustrated in Appendix B.5.

TABLE 5.4: Temporal Soot Gradient

Fuel	Unit	Cond. 1	Cond. 2	Cond. 3
DRef	$\mu\text{g}_{\text{soot}}/\text{ms}$	n.d.	179.8	235.1
G15	$\mu\text{g}_{\text{soot}}/\text{ms}$	n.d.	165.5	234.3
T25	$\mu\text{g}_{\text{soot}}/\text{ms}$	n.d.	107.0	160.4



## Chapter 6

# Discussion

In this chapter the results of both test rigs are discussed regarding the use of glycerol as a soot reducing fuel blend.

### Ignitability of Glycerol

Both experimental campaigns show an increased ignition delay time with the addition of glycerol. This behaviour is expected due to the low ignitability of glycerol and has already been reported by Eaton et al. [6]. With rising ambient gas temperatures and engine load, the ignition delay time decreases for both the G15 and the DRef. Interestingly, the difference in ignition delay is nearly constant among different conditions. This could be observed in the Instrumented Engine and in the Optical Engine with only the highest load condition without turbocharge in the Instrumented Engine showing convergence between the fuels. As the decrease in IDT of the G15 is equal to the decrease of the DRef, it is deduced that a significant increase in ignitability of the glycerol could not be achieved within the tested operating conditions. The consistency of observed effects on IDT across the two test rigs strengthens the reliability.

### Mechanisms of Soot Reduction

One aim of the study was to investigate whether the soot reducing effect of glycerol is chemically based or driven by physical parameters. Therefore, the spatial soot gradient SSG and the temporal soot gradient TSG are considered, which represent the maximal soot increase within 19 mm from the flame lift-off length and within 0.3 ms after ignition, respectively.

The relation of the SSG to the FLOL is necessary to take the different flame location into account. If using a fixed distance from the injector nozzle, a high-sooting fuel with a long FLOL would not be identified because the soot production might occur downstream from the fixed distance.

Relating the temporal soot gradient to ignition is more disputable because the ignition delay time has contrary effects on the TSG. On the one hand, a prolonged ignition delay decreases the local equivalence ratio and thus results in a lower TSG. On the other hand, the increased mixing time generates an enhanced premixed combustion rate and therefore a higher TSG. In the present study, the TSG is related to ignition, thereby also increasing comparability between different conditions.

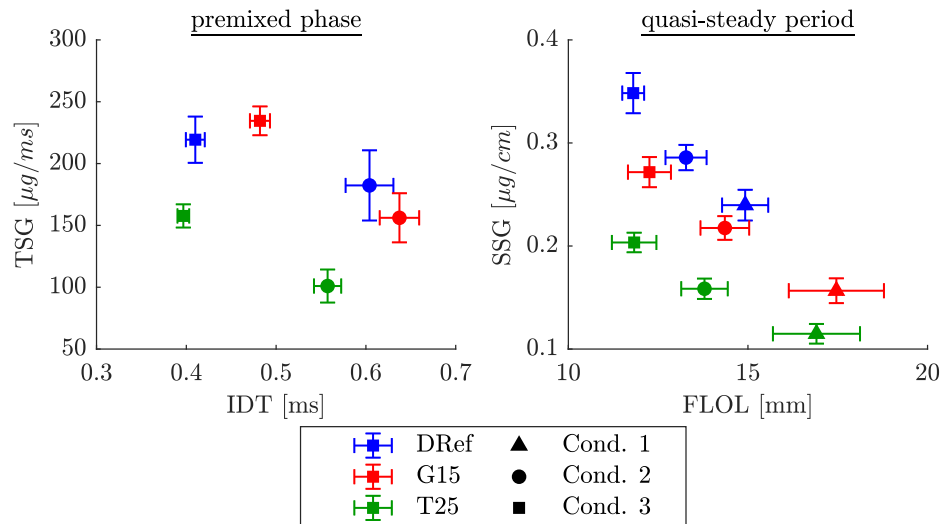


FIGURE 6.1: Temporal and spatial soot gradient plotted over ignition delay time and flame lift-off length; the bars represent the 95 % confidence interval

Figure 6.1 shows the temporal soot gradient plotted over ignition delay time on the left side and the spatial soot gradient over the flame lift-off length on the right side. The bars represent the 95 % confidence interval of each quantity. Regarding the premixed phase, the glycerol emulsion and the reference diesel feature no clear difference in sooting behaviour as the TSG confidence intervals are overlapping largely. At the high temperature condition, the glycerol emulsion shows a TSG even higher than the DRef, which is considered to be caused by above mentioned increased premixed combustion rate. The T25 fuel mixture with the benchmark additive TPGME shows the expected soot reducing behaviour [18, 21] with the TSG measurements being clearly separated from the DRef and the G15. With very similar ignition delay times at the highest condition, any effects due to more time for mixing can be ruled out for the T25.

During the quasi-steady period, a more significant difference between the glycerol emulsion and the pure reference diesel can be observed. With the glycerol featuring an increased flame lift-off length, it also shows a significantly lower spatial soot gradient. The decrease in SSG is consistent over all conditions, although the differences in FLOL decrease with rising ambient gas temperatures. This indicates that the soot reduction effect of the glycerol is not only physically driven. However, the glycerol emulsion is again clearly separated from the T25, which features the identical oxygen ratio.

This leads to the conclusion that the glycerol does not provide its inherent oxygen as effective as the TPGME to reduce in-flame soot. It is considered to be caused by the low reactivity of the glycerol. Demanding more energy to release its bond oxygen would explain, why the G15 cannot reduce soot production as effective as the T25.



## PM-CO Trade-off

Having a look at the engine-out emissions of the Instrumented Engine, the addition of glycerol yields a massive increase of particulate matter with diameters smaller than 10 nm and a reduction in the diameter range of greater than 25 nm. The properties and the origin of the small particles is yet to be determined. Regarding particle emissions with diameters greater than 25 nm, the reduction is most significant at low engine loads. However, the beneficial PM reduction effect is accompanied by an increase in carbon monoxide emissions. This trade-off is illustrated in Figure 6.2, which shows the CO emissions plotted over the number of emitted particles with diameters greater than  $d_p > 25$  nm. Both quantities are presented on a brake specific basis, while the marker size indicates the direction of rising engine loads.

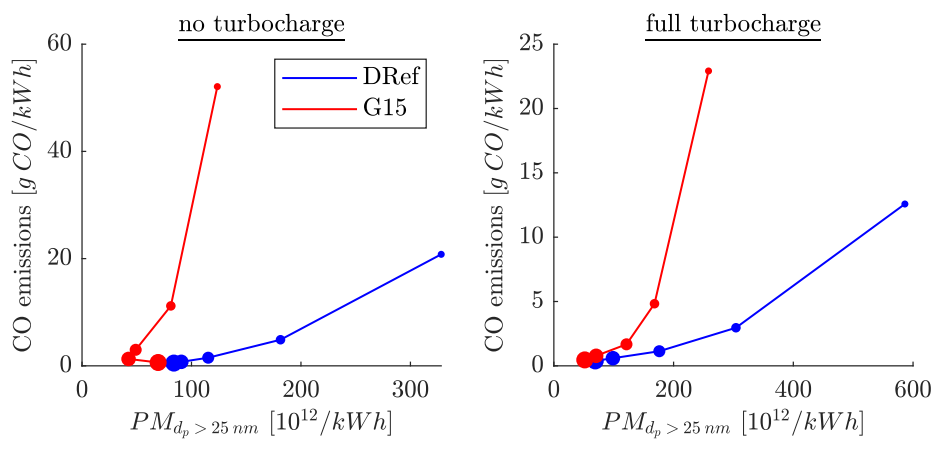


FIGURE 6.2: Brake specific CO emissions plotted over brake specific number of particles with diameters greater than  $d_p > 25$  nm

Brake specific CO and PM emissions are highest at the lowest load condition and decrease with increasing engine torque. Comparing the emissions for each condition, the glycerol yields a reduction in PM as shown by the horizontal displacement to the blue graph, but also features increased CO emissions illustrated by the vertical displacement. While the  $PM_{d_p > 25 \text{ nm}}$  reduction is most effective at low load conditions, the CO increase is likewise. This correlation is illustrated in Figure 6.3, which shows the ratio between the brake specific G15 and the DRef emissions. The engine load is indicated by the marker size and the dashed lines represent identical behaviour in each category.

With decreasing engine load, the ratio of  $PM_{d_p > 25 \text{ nm}}$  decreases and CO ratio increases. This trade-off is interpreted as the cause of glycerol's low reactivity. As soot is produced when the reaction is taking place too fast for mixing mechanisms to supply sufficient oxygen, decreasing reactivity results in a soot reduction. On the other hand, decreasing reactivity also slows down the conversion rate apart from the soot formation zone, therefore resulting in increased gaseous incomplete combustion products like CO. With increasing engine load, the combustion temperatures rise which enhance the reaction rate. Therefore, differences in PM and CO reduce with increasing engine load.

The increase of CO emissions of around 20 % at high load conditions is regarded as a minor concern because absolute values of carbon monoxide exhaust concentrations

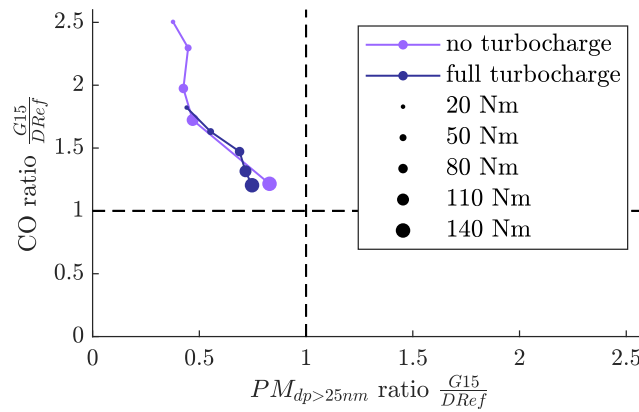


FIGURE 6.3: Ratio of brake specific CO emissions plotted over the ratio of brake specific  $PM_{dp>25nm}$  emissions

are low. In contrast to that, CO concentration is critical at low load conditions, which is why the large  $PM_{dp>25nm}$  reduction has to be put into perspective to the significant CO increase. Additionally, the toxic acrolein, which is formed under the thermal decomposition of glycerol and could not be assessed with present measurement equipment, is hypothesized to be consumed under efficient combustion conditions [20]. With carbon monoxide being an indicator of combustion incompleteness, it is recommended to avoid high CO emitting conditions if using glycerol as a fuel blend.

In conclusion, glycerol as a fuel blend is found to have a beneficial effect on particulate matter emissions with diameters greater than 25 nm but features a significant increase in particles smaller than 25 nm in diameter. Furthermore, an inverse correlation between CO and  $PM_{dp>25nm}$  is observed.

## Chapter 7

# Conclusions and Perspectives

The experimental investigations on a 15 w% glycerol-diesel emulsion conducted on an instrumented and an optical engine have shown stable combustion. The preparation method of the emulsion resulted in satisfactory stability for an examination within 12 hours. Comparing the combustion properties and emissions of the glycerol emulsion to the reference diesel, the following characteristics are observed:

- Engine operation with an adjusted combustion timing of 50 % cumulative heat release indicates the same brake thermal efficiency.
- The glycerol emulsion features a prolonged ignition delay which is present across all load and temperature conditions.
- The glycerol emulsion shows higher maximal heat release rates.
- The addition of glycerol results in an increased flame lift-off length at the low ambient gas temperature condition and shows no difference at the high temperature condition.
- A large peak of particulate matter in the diameter range of 5 nm to 10 nm is observed when measuring the engine-out emissions. The peak is present across all operating conditions and differs from the reference diesel emissions by two orders of magnitude.
- A reduction of particle emissions with more than 25 nm in diameter is achieved, which ranges between 62 % at the lowest engine load and 17 % at the highest engine load. This behaviour is consistent with the in-flame soot measurements during the quasi-steady combustion period.
- Carbon monoxide emissions increase by a factor of 2.5 at low loads and by 1.2 at high loads. An inverse correlation is observed between carbon monoxide and the emission of particles with more than 25 nm in diameter.
- The comparison to a 25 w% TPGME-diesel fuel mixture showed that the glycerol provides its inherent oxygen less effectively to reduce soot formation.

The reduction of in-flame soot and large particulate matter emissions are considered to be caused partly by the fuel oxygen content, while large reductions at low temperature and low load conditions are related to physically increased air fuel mixing. The low reactivity of glycerol provides more time for air fuel mixing and contributes to soot reduction. Simultaneously, it results in an increase of incomplete combustion products. Both effects are most significant at low temperature operating conditions and decrease with increasing load, turbocharge, and ambient gas temperature. The reduction observed at high temperature operating conditions, where the impact of

the fuel reactivity is minor, is considered to be caused by the oxygen content of the glycerol.

Further investigation on the reaction kinetics of glycerol-diesel emulsions will be conducted based on numerical simulations. A premixed combustion model is expected to provide more information on the chemical effects of glycerol on soot formation. Reaction kinetics will also be analysed with regard to the observed higher heat release rates of glycerol.

Additionally, the origin of the large increase of particulate matter emissions in the diameter range below 10 nm is yet to be identified. Since the samples of exhaust particulates indicate that the glycerol features an increased non-soot fraction, numerical simulations will be used to examine whether a large increase of volatile species is observed. Moreover, the collected exhaust samples will be analysed with transmission electron microscopy regarding their structure, which is expected to provide further information about the particles' origin.

In conclusion, the study has shown that usage of abundant glycerol as a diesel fuel blend is possible but also revealed a new challenge with the large increase of small particle emissions. Apart from the latter, the impact on the emissions can be summarised as a trade-off between soot reduction and an increase of incomplete combustion products.

## **Appendix A**

# **Fuel Analysis Sheets**

### Certificate of Analysis

<b>Fuel Batch No:</b>	CAF-G19/1229	<b>Contact:</b>	David Emberson
<b>Fuel Description:</b>	EN590 B0 Additive Free	<b>Order No:</b>	N1925731
<b>Part No:</b>	10000085	<b>Customer:</b>	NTNU
		<b>Date:</b>	02/04/2019

Test	Method	Unit	Limit		Result
			Min	Max	
Appearance	Visual		Report		C&B
Cetane Number *	EN ISO 5165		51.0	-	60.4
Cetane Index	EN ISO 4264		46.0	-	58.4
Density @ 15°C #	EN ISO 12185	kg/L	0.8200	0.8450	0.8230
Cloud Point *	EN ISO 23015	°C	-	-7	-11
CFPP	EN 116	°C	Report		-13
Flash Point #	EN ISO 2719	°C	55.0	-	90.5
Lubricity, wear scar diameter @ 60°C *	EN ISO 12156-1	µm	Report		623
Sulfur #	EN ISO 20846	mg/kg	-	10.0	1.4
Viscosity at 40°C #	EN ISO 3104	mm²/s	2.000	4.500	2.534
Water Content	EN ISO 12937	mg/kg	-	200	60
FAME Content	EN 14078	% m/m	-	0.1	<0.1
Mono Aromatics Content	IP 391 mod	% m/m	Report		12.0
Di Aromatics Content	IP 391 mod	% m/m	Report		6.1
Tri+ Aromatics Content	IP 391 mod	% m/m	Report		0.0
Polycyclic Aromatics Content	IP 391 mod	% m/m	-	8.0	6.1
Total Aromatics	IP 391 mod	% m/m	Report		18.1
Oxidation Stability (16h)	EN ISO 12205	g/m³	-	25	<1
Ash Content	EN ISO 6245	% m/m	-	0.010	<0.001
Carbon Residue (10% Dis. Res)	EN ISO 10370	% m/m	-	0.30	<0.01
Copper Corrosion (3h at 50°C)	EN ISO 2160	Rating	Class 1	-	1A
Total Contamination	EN 12662	mg/kg	-	24	<6
Manganese *	MT/ELE/15	mg/kg	Report		<0.004
Gross Calorific Value	ASTM D3338 mod	MJ/kg	Report		46.27
Net Calorific Value	ASTM D3338 mod	MJ/kg	Report		43.33

**Certificate of Analysis**

<b>Fuel Batch No:</b>	CAF-G19/1229	<b>Contact:</b>	David Emberson
<b>Fuel Description:</b>	EN590 B0 Additive Free	<b>Order No:</b>	N1925731
<b>Part No:</b>	10000085	<b>Customer:</b>	NTNU
		<b>Date:</b>	02/04/2019

Test	Method	Unit	Limit		Result
			Min	Max	
Distillation (Evaporated) #					
E250	EN ISO 3405	% v/v	-	65.0	30.8
E350	EN ISO 3405	% v/v	85.0	-	95.8
IBP	EN ISO 3405	°C		Report	211.9
10% Volume Evaporated	EN ISO 3405	°C		Report	233.1
20% Volume Evaporated	EN ISO 3405	°C		Report	241.5
30% Volume Evaporated	EN ISO 3405	°C		Report	249.4
40% Volume Evaporated	EN ISO 3405	°C		Report	256.0
50% Volume Evaporated	EN ISO 3405	°C		Report	261.3
60% Volume Evaporated	EN ISO 3405	°C		Report	266.3
70% Volume Evaporated	EN ISO 3405	°C		Report	272.1
80% Volume Evaporated	EN ISO 3405	°C		Report	280.8
90% Volume Evaporated	EN ISO 3405	°C		Report	304.0
95% Volume Evaporated	EN ISO 3405	°C	-	360.0	342.0
FBP	EN ISO 3405	°C		Report	364.3
Residue	EN ISO 3405	% v/v		Report	1.3

# Test UKAS accredited \* Test performed by sub-contracted laboratory

**Sample Received Condition:** Good (No Seal)  
**Date Sample Received:** 25/03/2019

**Notes:**

**Date:** 02/04/2019  
**Authorised by:** M Babiarz  
*Fuels Formulation Scientist*

Coryton Advanced Fuels Ltd  
The Manorway  
Stanford-le-Hope  
Essex SS17 9LN, UK

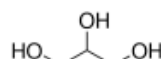
Tel: +44 (0)1375 665930  
Email: lab@corytonfuels.co.uk  
Website: www.corytonfuels.co.uk



## Certificate of Analysis

Product Name:  
Glycerol - >99%, FCC, FG

**Product Number:** W252506  
**Batch Number:** MKCG0567  
**Brand:** ALDRICH  
**CAS Number:** 56-81-5  
**MDL Number:** MFCD00004722  
**Formula:** C3H8O3  
**Formula Weight:** 92.09 g/mol  
**Quality Release Date:** 13 MAR 2018  
**Expiration Date:** FEB 2023



Test	Specification	Result
Appearance (Color)	Colorless	Colorless
Appearance (Form)	Viscous Liquid	Viscous Liquid
Infrared Spectrum	Conforms to Structure	Conforms
Color Test	Pass	Pass
Purity (GC)	≥ 99.0 %	99.7 %
Water (by Karl Fischer)	≤ 1.0 %	0.1 %
Residue on ignition (Ash)	≤ 0.01 %	< 0.01 %
Specific Gravity	≥ 1.259	1.260
Subs Carbonizable by Hot H2SO4	Pass	Pass
Miscellaneous Assay	Pass	Pass
Fatty Acid Ester Test		
Chlorine Compounds	≤ 0.003 %	< 0.003 %
Arsenic (As)	≤ 3.0 ppm	< 0.2 ppm
Cadmium (Cd)	≤ 1.0 ppm	< 0.1 ppm
Mercury (Hg)	≤ 1.0 ppm	< 0.1 ppm
Lead (Pb)	≤ 1.0 ppm	< 0.1 ppm
Expiration Date Period	-----	-----
5 Years		

Michael Grady, Manager  
Quality Control

Sigma-Aldrich warrants, that at the time of the quality release or subsequent retest date this product conformed to the information contained in this publication. The current Specification sheet may be available at Sigma-Aldrich.com. For further inquiries, please contact Technical Service. Purchaser must determine the suitability of the product for its particular use. See reverse side of invoice or packing slip for additional terms and conditions of sale.



---

3050 Spruce Street, Saint Louis, MO 63103, USA

Website: [www.sigmaaldrich.com](http://www.sigmaaldrich.com)

Email USA: [techserv@sial.com](mailto:techserv@sial.com)

Outside USA: [eurtechserv@sial.com](mailto:eurtechserv@sial.com)

## Certificate of Analysis

**Product Number:** W252506  
**Batch Number:** MKCG0567

---

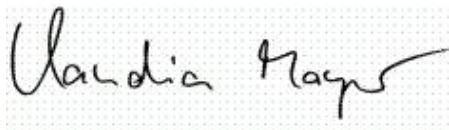
Milwaukee, WI US

Sigma-Aldrich warrants, that at the time of the quality release or subsequent retest date this product conformed to the information contained in this publication. The current Specification sheet may be available at [Sigma-Aldrich.com](http://Sigma-Aldrich.com). For further inquiries, please contact Technical Service. Purchaser must determine the suitability of the product for its particular use. See reverse side of invoice or packing slip for additional terms and conditions of sale.

## Certificate of Analysis

**Product Name:** TRI(PROPYLENE GLYCOL) METHYL ETHER, MIXTURE OF ISOMERS  
>= 97.5 %  
**Product Number:** 484245  
**Batch Number:** STBJ0184  
**Brand:** Aldrich  
**CAS Number:** 25498-49-1  
**Formula:** CH<sub>3</sub>(OC<sub>3</sub>H<sub>6</sub>)<sub>3</sub>OH  
**Formula Weight:** 206.28  
**Quality Release Date:** 15 JAN 2019

TEST	SPECIFICATION	RESULT
APPEARANCE (COLOR)	COLORLESS	COLORLESS
APPEARANCE (FORM)	LIQUID	LIQUID
COLOR (IN APHA)	≤ 15 APHA	< 15 APHA
PURITY (GC AREA %)	≥ 97.5 %	98.1 %
REMARKS ON GC	AS A MIXTURE OF ISOMERS	AS A MIXTURE OF ISOMERS
WATER	≤ 0.1 %	< 0.1 %
INFRARED SPECTRUM	CONFORMS TO STRUCTURE	CONFORMS



Claudia Mayer  
Manager Quality Control  
Steinheim, Germany

Sigma-Aldrich warrants that at the time of the quality release or subsequent retest date this product conformed to the information contained in this publication. The current specification sheet may be available at Sigma-Aldrich.com. For further inquiries, please contact Technical Service. Purchaser must determine the suitability of the product for its particular use. See reverse side of invoice or packing slip for additional terms and conditions of sale.

## Appendix B

# Optical Engine Results

### B.1 Tune Compression Ratio for In-Cylinder Gas Temperature Estimation

TABLE B.1: Calibration map for the Tuned Compression Ratio

No.	$p_{in}$ [bar]	$T_{in}$ [°C]	$p_{TDC\,mea.}$ [bar]	$p_{TDC\,mod.}$ [bar]	$T_{TDC\,mod.}$ [K]	$\rho_{TDC\,mod.}$ [kg/m <sup>3</sup> ]	CR [–]
1	1.30	50.0	39.88	39.88	798.9	17.39	12.40
2	1.30	80.1	38.89	38.89	850.2	15.93	12.42
3	1.30	99.9	38.20	38.20	882.7	15.07	12.41
4	1.30	130.0	37.43	37.43	931.5	13.99	12.45
5	1.40	50.0	43.11	43.11	800.0	18.77	12.43
6	1.40	80.0	42.02	42.02	851.3	17.19	12.44
7	1.40	100.0	41.28	41.28	884.2	16.26	12.43
8	1.40	130.1	40.18	40.18	931.9	15.02	12.40
9	1.50	49.9	46.19	46.19	800.2	20.11	12.42
10	1.50	80.0	45.14	45.14	852.4	18.45	12.46
11	1.50	100.0	44.27	44.28	884.9	17.43	12.43
12	1.50	130.0	43.24	43.25	933.6	16.13	12.44

## B.2 Ignition Delay Time

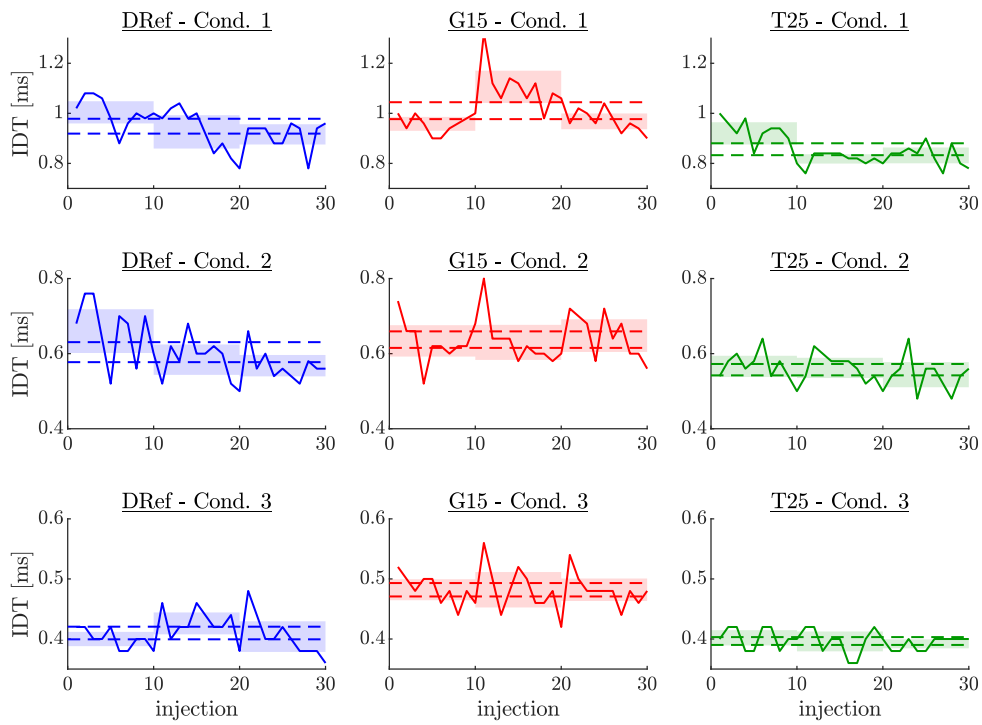


FIGURE B.1: Ignition delay time: Shaded area represents the 95 % confidence interval of each 10 consecutive recorded injections. The dashed interval shows the 95 % confidence interval of all injections.

### B.3 Flame Lift-off Length

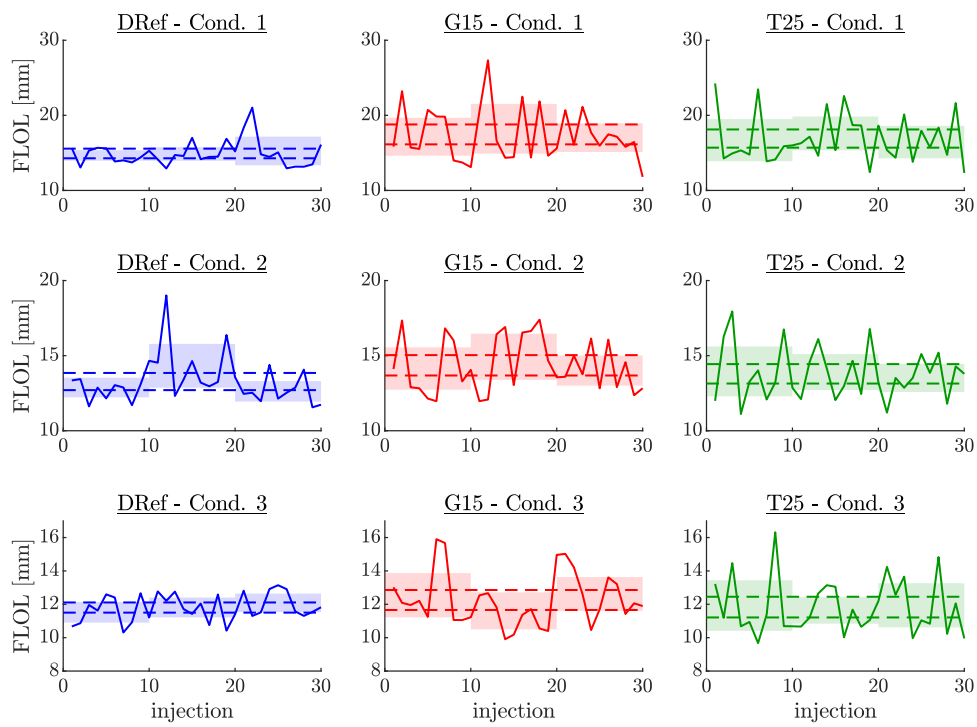


FIGURE B.2: Flame lift-off length: Shaded area represents the 95 % confidence interval of each 10 consecutive recorded injections. The dashed interval shows the 95 % confidence interval of all injections.

## B.4 Spatial Soot Gradient

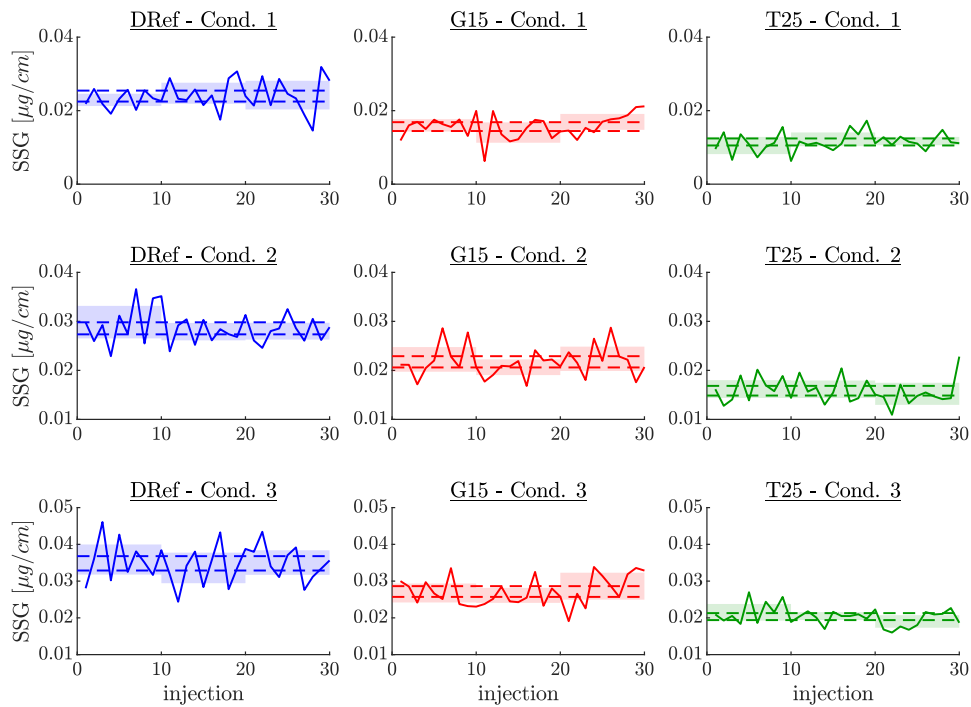


FIGURE B.3: Spatial soot gradient: Shaded area represents the 95 % confidence interval of each 10 consecutive recorded injections. The dashed interval shows the 95 % confidence interval of all injections.

## B.5 Temporal Soot Gradient

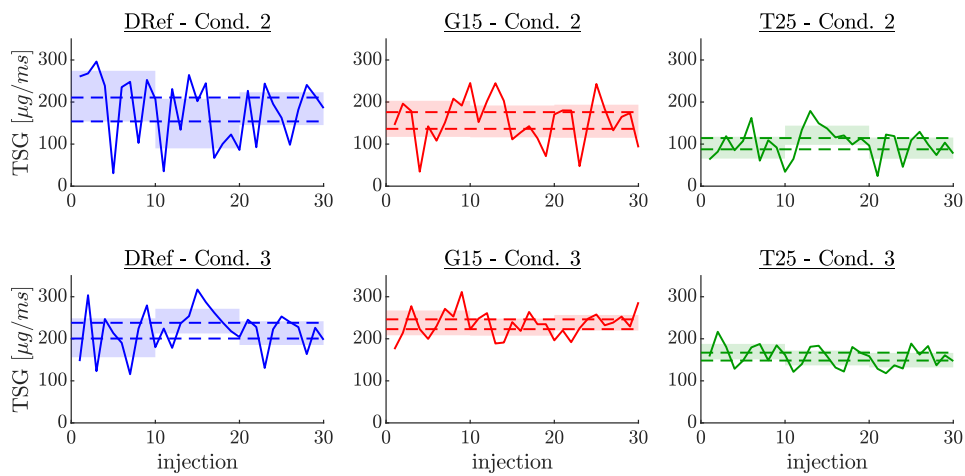


FIGURE B.4: Temporal soot gradient: Shaded area represents the 95 % confidence interval of each 10 consecutive recorded injections. The dashed interval shows the 95 % confidence interval of all injections.

# Bibliography

- [1] European Parliament and Council of the European Union, "Directive 2008/50/EC of the European Parliament and of the Council of 21 May 2008 on ambient air quality and cleaner air for Europe", *Official Journal of the European Union*, volume L 152, pages 1–44, Jun. 2008. [Online]. Available: <http://data.europa.eu/eli/dir/2008/50/oj>.
- [2] European Parliament and Council of the European Union, "Regulation (EC) No 715/2007 of the European Parliament and of the Council of 20 June 2007 on type approval of motor vehicles with respect to emissions from light passenger and commercial vehicles (Euro 5 and Euro 6) and on access to vehicle repair and maintenance information", *Official Journal of the European Union*, volume L 171, pages 1–16, Jun. 2007. [Online]. Available: <http://data.europa.eu/eli/reg/2007/715/oj>.
- [3] European Parliament and Council of the European Union, "Regulation (EU) 2018/858 of the European Parliament and of the Council of 30 May 2018 on the approval and market surveillance of motor vehicles and their trailers, and of systems, components and separate technical units intended for such vehicles, amending Regulations (EC) No 715/2007 and (EC) No 595/2009 and repealing Directive 2007/46/EC", *Official Journal of the European Union*, volume L 151, pages 1–218, Jun. 2018. [Online]. Available: <http://data.europa.eu/eli/reg/2018/858/oj>.
- [4] A. Cornejo, I. Barrio, M. Campoy, J. Lázaro, and B. Navarrete, "Oxygenated fuel additives from glycerol valorization. Main production pathways and effects on fuel properties and engine performance: A critical review", *Renewable and Sustainable Energy Reviews*, volume 79, pages 1400–1413, Nov. 2017. DOI: 10.1016/j.rser.2017.04.005.
- [5] J. A. Melero, G. Vicente, G. Morales, M. Paniagua, and J. Bustamante, "Oxygenated compounds derived from glycerol for biodiesel formulation: Influence on EN 14214 quality parameters", *Fuel*, volume 89, number 8, pages 2011–2018, 2010. DOI: 10.1016/j.fuel.2010.03.042.
- [6] S. J. Eaton, G. N. Harakas, R. W. Kimball, J. A. Smith, K. A. Pilot, M. T. Kufflik, and J. M. Bullard, "Formulation and Combustion of Glycerol–Diesel Fuel Emulsions", *Energy & Fuels*, volume 28, number 6, pages 3940–3947, Jun. 2014. DOI: 10.1021/ef500670d.
- [7] M. S. Sidhu, M. M. Roy, and W. Wang, "Glycerine emulsions of diesel-biodiesel blends and their performance and emissions in a diesel engine", *Applied Energy*, volume 230, pages 148–159, Nov. 2018. DOI: 10.1016/j.apenergy.2018.08.103.
- [8] K.-H. Kim, E. Kabir, and S. Kabir, "A review on the human health impact of airborne particulate matter", *Environment International*, volume 74, pages 136–143, Jan. 2015. DOI: 10.1016/j.envint.2014.10.005.
- [9] J. B. Heywood, *Internal Combustion Engine Fundamentals*, series Automotive technology. McGraw Hill, 1988, ISBN: 0-07-100499-8.

- [10] H. Omidvarborna, A. Kumar, and D.-S. Kim, "Recent studies on soot modeling for diesel combustion", *Renewable and Sustainable Energy Reviews*, volume 48, pages 635–647, Aug. 2015. DOI: 10.1016/j.rser.2015.04.019.
- [11] J. E. Dec, "Advanced compression-ignition engines—understanding the in-cylinder processes", *Proceedings of the Combustion Institute*, volume 32, number 2, pages 2727–2742, Jan. 2009. DOI: 10.1016/j.proci.2008.08.008.
- [12] S. Pischinger, *Internal Combustion Engines II*, 8th edition. Aachen: Institute for Combustion Engines - RWTH Aachen University, 2013.
- [13] B. Graziano, "Determination of Characteristic Fuel Numbers to Assess Bio-fuels Sooting Behavior in Compression Ignition Engines", Doctoral Thesis, RWTH Aachen University, Aachen, 2018.
- [14] C. J. Mueller, W. J. Pitz, L. M. Pickett, G. C. Martin, D. L. Siebers, and C. K. Westbrook, "Effects of Oxygenates on Soot Processes in DI Diesel Engines: Experiments and Numerical Simulations", *SAE Transactions*, volume 112, pages 964–982, 2003, ISSN: 0096-736X.
- [15] J. Reijnders, M. Boot, and P. de Goey, "Impact of aromaticity and cetane number on the soot-NO<sub>x</sub> trade-off in conventional and low temperature combustion", *Fuel*, volume 186, pages 24–34, Dec. 2016. DOI: 10.1016/j.fuel.2016.08.009.
- [16] National Institute of Standards and Technology, U.S. Department of Commerce, *Glycerin*, 2018. [Online]. Available: [https://webbook.nist.gov/cgi/inchi/InChI%3D1S/C3H8O3/c4-1-3\(6\)2-5/h3-6H%2C1-2H2](https://webbook.nist.gov/cgi/inchi/InChI%3D1S/C3H8O3/c4-1-3(6)2-5/h3-6H%2C1-2H2) (visited on 07/17/2019).
- [17] H. Y. Setyawan, M. Zhu, Z. Zhang, and D. Zhang, "Ignition and combustion characteristics of single droplets of a crude glycerol in comparison with pure glycerol, petroleum diesel, biodiesel and ethanol", *Energy*, volume 113, pages 153–159, Oct. 2016. DOI: 10.1016/j.energy.2016.07.032.
- [18] C. E. Dumitrescu, A. S. Cheng, E. Kurtz, and C. J. Mueller, "A Comparison of Methyl Decanoate and Tripropylene Glycol Monomethyl Ether for Soot-Free Combustion in an Optical Direct-Injection Diesel Engine", *Journal of Energy Resources Technology*, volume 139, number 4, page 042210, Jul. 2017. DOI: 10.1115/1.4036330.
- [19] PubChem, *Tripropylene glycol methyl ether*. [Online]. Available: <https://pubchem.ncbi.nlm.nih.gov/compound/25054> (visited on 08/15/2019).
- [20] C. R. Coronado, J. A. Carvalho, C. A. Quispe, and C. R. Sotomonte, "Ecological efficiency in glycerol combustion", *Applied Thermal Engineering*, volume 63, number 1, pages 97–104, Feb. 2014. DOI: 10.1016/j.applthermaleng.2013.11.004.
- [21] J. Manin, S. Skeen, L. Pickett, E. Kurtz, and J. E. Anderson, "Effects of Oxygenated Fuels on Combustion and Soot Formation/ Oxidation Processes", *SAE International Journal of Fuels & Lubricants*, volume 7, number 3, pages 704–717, Nov. 2014. DOI: 10.4271/2014-01-2657.
- [22] Y. Wang and B. Zhang, *Biomass Processing, Conversion, and Biorefinery*. Hauppauge, New York: Nova Science Publishers, Inc, 2013, ISBN: 978-1-62618-346-9.
- [23] C. A. G. Quispe, C. J. R. Coronado, and J. A. Carvalho Jr., "Glycerol: Production, consumption, prices, characterization and new trends in combustion", *Renewable and Sustainable Energy Reviews*, volume 27, pages 475–493, Nov. 2013. DOI: 10.1016/j.rser.2013.06.017.
- [24] S. A. Steinmetz, J. S. Herrington, C. K. Winterrowd, W. L. Roberts, J. O. L. Wendt, and W. P. Linak, "Crude glycerol combustion: Particulate, acrolein, and other volatile organic emissions", *Proceedings of the Combustion Institute*,



- volume 34, number 2, pages 2749–2757, Jan. 2013. DOI: 10.1016/j.proci.2012.07.050.
- [25] J. McNeil, P. Day, and F. Sirovski, “Glycerine from biodiesel: The perfect diesel fuel”, *Process Safety and Environmental Protection*, volume 90, number 3, pages 180–188, May 2012. DOI: 10.1016/j.psep.2011.09.006.
- [26] FIA Formula E, *INSIGHT: Formula E’s emission-free charging*, Jun. 2016. [Online]. Available: <http://www.fiaformulae.com/en/news/2016/june/insight-formula-e-s-emission-free-charging/> (visited on 07/01/2019).
- [27] B. K. Debnath, U. K. Saha, and N. Sahoo, “A comprehensive review on the application of emulsions as an alternative fuel for diesel engines”, *Renewable and Sustainable Energy Reviews*, volume 42, pages 196–211, Feb. 2015. DOI: 10.1016/j.rser.2014.10.023.
- [28] S. J. Eaton, T. T. Wallace, B. G. Sarnacki, T. L. Adams, R. W. Kimball, J. A. Henry, and G. N. Harakas, “Combustion and emissions of a glycerol-biodiesel emulsion fuel in a medium-speed engine”, *Journal of Marine Engineering & Technology*, volume 18, number 2, pages 102–111, May 2019. DOI: 10.1080/20464177.2018.1507429.
- [29] K. O. P. Bjørgen, D. R. Emberson, and T. Løvås, “Optical Measurements of In-Flame Soot in Compression-Ignited Methyl Ester Flames”, *Energy & Fuels*, volume 33, number 8, pages 7886–7900, Aug. 2019. DOI: 10.1021/acs.energyfuels.9b01467.
- [30] Cambustion Ltd, *Cambustion DMS500 MkII*, Mar. 2019. [Online]. Available: <https://www.cambustion.com/sites/default/files/instruments/DMS500/DMS500engine.pdf>.
- [31] Z. Žák, M. Emrich, M. Takáts, and J. Macek, “In-Cylinder Heat Transfer Modelling”, *Journal of Middle European Construction and Design of Cars*, volume 14, number 3, pages 2–10, Dec. 2016. DOI: 10.1515/mecdc-2016-0009.
- [32] B. J. G. McBride, “Coefficients for calculating thermodynamic and transport properties of individual species”, Tech. Rep., Oct. 1993. [Online]. Available: <https://ntrs.nasa.gov/search.jsp?R=19940013151>.
- [33] C. F. Bohren and D. R. Huffman, *Absorption and Scattering of Light by Small Particles*. John Wiley & Sons, Apr. 1998, ISBN: 978-0-471-29340-8.
- [34] S. Skeen, K. Yasutomi, E. Cenker, B. Adamson, N. Hansen, and L. Pickett, *Standardized optical constants for soot quantification in high-pressure sprays*, Apr. 2018. DOI: 10.4271/2018-01-0233.
- [35] B. Higgins and D. Siebers, “Measurement of the Flame Lift-Off Location on DI Diesel Sprays Using OH Chemiluminescence”, *SAE Transactions*, volume 110, pages 739–753, 2001, ISSN: 0096-736X.
- [36] K. O. P. Bjørgen, D. R. Emberson, and T. Lovas, “Diffuse Back-Illuminated Extinction Imaging of Soot: Effects of Beam Steering and Flame Luminosity”, Jan. 2019. DOI: 10.4271/2019-01-0011.
- [37] F. R. Westlye, K. Penney, A. Ivarsson, L. M. Pickett, J. Manin, and S. A. Skeen, “Diffuse back-illumination setup for high temporally resolved extinction imaging”, *Applied Optics*, volume 56, number 17, pages 5028–5038, Jun. 2017. DOI: 10.1364/AO.56.005028.
- [38] J. Manin, S. A. Skeen, and L. M. Pickett, “Performance comparison of state-of-the-art high-speed video cameras for scientific applications”, *Optical Engineering*, volume 57, number 12, page 124105, Dec. 2018. DOI: 10.1117/1.OE.57.12.124105.

- [39] M. Lapuerta, R. Ballesteros, and J. Rodríguez-Fernández, "Thermogravimetric analysis of diesel particulate matter", *Measurement Science and Technology*, volume 18, number 3, pages 650–658, Jan. 2007. DOI: 10.1088/0957-0233/18/3/015.
- [40] M. Gibbons Natrella, *Experimental Statistics - 2.1.5 Confidence Interval*. Dover Publications, 2005, ISBN: 978-0-486-43937-2.

